Design, Implementation, and Medical Applications of 2-D Ultrasound Sparse Arrays

Alessandro Ramalli, *Senior Member, IEEE*, Enrico Boni, *Member, IEEE*, Emmanuel Roux, Hervé Liebgott, and Piero Tortoli, *Fellow, IEEE*

***Abstract*— An ultrasound sparse array consists of a sparse distribution of elements over a 2-D aperture. Such an array is typically characterized by a limited number of elements, which in most cases is compatible with the channel number of the available scanners. Sparse arrays represent an attractive alternative to full 2-D arrays that may require the control of thousands of elements through expensive application-specific integrated circuits (ASICs). However, their massive use is hindered by two main drawbacks: the possible beam profile deterioration, which may worsen the image contrast, and the limited signal-to-noise ratio (SNR), which may result too low for some applications. This article reviews the work done for three decades on 2-D ultrasound sparse arrays for medical applications. First, random, optimized, and deterministic design methods are reviewed together with their main influencing factors. Then, experimental 2-D sparse array implementations based on piezoelectric and capacitive micromachined ultrasonic transducer (CMUT) technologies are presented. Sample applications to 3-D (Doppler) imaging, super-resolution imaging, photo-acoustic imaging, and therapy are reported. The final sections discuss the main shortcomings associated with the use of sparse arrays, the related countermeasures, and the next steps envisaged in the development of innovative arrays.**

***Index Terms*— 2-D arrays, 3-D ultrasound imaging, capacitive micromachined ultrasonic transducer (CMUT), genetic algorithm (GA), piezoelectric, simulated annealing (SA), sparse arrays, spiral arrays, transducers.**

I. Introduction

THE introduction of 2-D arrays has greatly boosted the development of novel ultrasound imaging methods aimed at scanning a full volume (3-D) in real time [1]. For several years, 3-D imaging had been done by moving a transducer array either manually or using a step motor [2], but, in both cases, poor temporal resolution was achieved. The 2-D arrays can rapidly scan a full volume through electronic steering [3], but require thousands of elements. So many elements can be controlled either through sophisticated and expensive application-specific integrated circuits (ASICs) performing the so-called micro-beamforming [3]–[7] or through a high number of transmission (TX) and reception (RX) channels. The first approach was implemented in high-end scanners [8], [9] and has been shown capable to perform impressive 3-D investigations. However, most research laboratories have no access to such machines and usually base their experimental work on the so-called open scanners [10], [11]. Open scanners are characterized by full flexibility in the control of transducer elements but typically have 64-256 TX/RX channels. Hence, to test novel 3-D imaging methods by a single (or a few, synchronized, [12]–[15]) open scanner(s), it is necessary to decrease the number of active elements in the 2-D array. Any method addressed to reduce the channel count without dramatically affecting the corresponding image quality is therefore appealing.

As an example, the row–column-addressed (RCA) arrays have been recently proposed [16]–[20]. In an RCA array, the elements of a full, 2-D, $N \times N$-element matrix are accessed by their row or column index. All the elements in a row are connected and, thereby, they act as one $1 \times N$ large element. Similarly, all the elements in a column are connected and act as one $N \times 1$ large element. Hence, these probes consist of two orthogonal overlapping linear arrays, each made up of N elongated elements, so that a total of $N + N$ elements cover the same square aperture of a 2-D $N \times N$-element matrix. RCA arrays can transmit and receive using alternatively either the rows or the columns. For example, by combining the TX from different rows and the RX by different columns an entire volume can be scanned. However, the classic delay and sum beamforming, which considers point sources, must be amended to consider the cylindrical sources emitted by the elongated elements [19].

On the other hand, a sparse array consists of a sparse distribution of elements over a 2-D aperture. Such elements are usually a subset of those available in a (gridded) matrix array but could also be the elements of an (ungridded) native-

Manuscript received 5 January 2022; accepted 20 March 2022. Date of publication 25 March 2022; date of current version 27 September 2022. This work was supported in part by the Moore4Medical Project through the Electronic Components and Systems for European Leadership (ECSEL) Joint Undertaking under Grant H2020-ECSEL-2019-IA-876190; and in part by the Frameworks of LABEX Physique, Radiobiologie, Imagerie Médicale et Simulation (PRIMES) under Grant ANR-10-LABX-0063 and LABEX Centre Lyonnais d'Acoustique (CELYA) under Grant ANR-10-LABX-0060, Université de Lyon, within the Program "Investissements d'Avenir" under Grant ANR-11-IDEX-0007 operated by the French National Research Agency (ANR). *(Corresponding author: Piero Tortoli.)*

Alessandro Ramalli, Enrico Boni, and Piero Tortoli are with the Department of Information Engineering, University of Florence, 50139 Florence, Italy (e-mail: piero.tortoli@unifi.it).

Emmanuel Roux and Hervé Liebgott are with Université de Lyon, INSA-Lyon, Université Claude Bernard Lyon 1, UJM-Saint Etienne, CNRS, Inserm, CREATIS UMR 5220, U1294, F-69100 Lyon, France.

Digital Object Identifier 10.1109/TUFFC.2022.3162419

This work is licensed under a Creative Commons Attribution-NonCommercial-NoDerivatives 4.0 License.
For more information, see https://creativecommons.org/licenses/by-nc-nd/4.0/

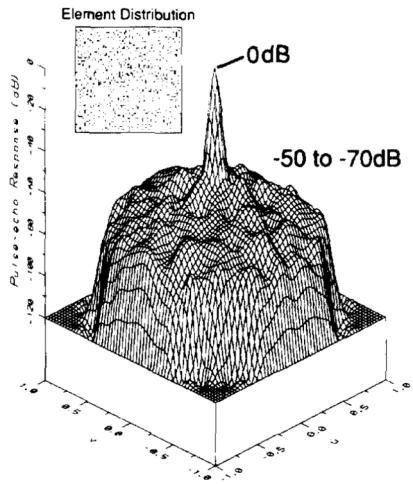

Fig. 1. Sixth-order sparse element distribution and corresponding on-axis beam profile, based on the design by Turnbull and Foster. © 1991 IEEE. Reprinted, with permission, from [23].

sparse array. In both cases, the key aspect is represented by the criterion used to design the position of the active elements.

This issue was first faced within the field of broadband electromagnetic antenna arrays [21], when it was suggested that by nonuniformly spacing an assigned number of antennas, advantages in terms of resolution (decreased main lobe width) or secondary lobe level (SLL) control can be obtained [22].

The possibility of using sparsity to reduce the channel count in association with ultrasonic 2-D arrays was first highlighted in the article by Turnbull and Foster [23]. They showed that when a random selection of elements was removed from a periodic dense array, the main lobe turned out to be practically unchanged, while the average SLL increased, see Fig. 1. In stochastic random sparse arrays [24]–[27], a limited set of configurations was initially defined by randomly choosing part of the elements of a fully populated 2-D array. The configuration yielding the best performance (e.g., in terms of beamwidth or of SLL) was then selected.

In the work by Weber *et al.* [28], substantial differences in the SLLs of different random patterns containing the same number of elements were highlighted. This finding encouraged the development of processes addressed to generate array patterns optimized for a given matrix array and order of reduction. Optimization is usually based on the minimization of a cost function, e.g., the difference between the radiation patterns of the random array and the fully sampled 2-D array. This minimization is typically achieved after thousands of iteration steps leading to patterns that are almost independent of the initial array pattern. Weber *et al.* [28] proposed to select the best sparse array layout by adopting a genetic algorithm (GA) based on the principles of evolution [29], [30]. Instead, in [31]–[40], the cost function was minimized through the simulated annealing (SA) algorithm. SA aims at simulating the behavior of a collection of atoms of a carefully cooled substance, which slowly forms an ideal crystal (minimum-energy state) [41].

Optimized designs usually require a high-computational cost and might be affected by convergence problems. This has encouraged the parallel development of deterministic approaches capable of providing suboptimal array designs. For example, different subsets of active elements in TX and RX arrays were considered for the cross-Mills arrays [42] and the sparse periodic layouts [27], [43]–[45]. Aperiodic layouts, based on spiral arrays, were also suggested in [46] and further developed in [47]–[49].

This article reviews the work done for over 30 years in the field of 2-D ultrasound sparse arrays, spanning from design approaches to implementations and medical applications, and aims at highlighting the related weaknesses and strengths.

Section II illustrates the main sparse array design methods. First, the main factors influencing such methods are described in Section II-A. Then, random, optimized, and deterministic methods are reviewed in Sections II-B–II-D, respectively. The experimental 2-D sparse array implementations based on piezoelectric and capacitive micromachined ultrasonic transducer (CMUT) technologies are reviewed in Sections III-A and III-B, respectively. The use of sparse arrays in applications ranging from 3-D (Doppler) imaging to photoacoustic imaging and therapy is reported in Section III-C. The main drawbacks associated with the use of sparse arrays are discussed in Section IV together with possible related countermeasures. The next steps envisaged in the development of innovative sparse arrays are included in the final Section V.

II. Design Methods

A. Generalities

The design of sparse arrays is influenced by several factors that can be grouped as follows.

1) Number/Weighting of Elements: In early studies on 2-D medical ultrasound sparse arrays [28], [29], [33], [50], [51], the number of elements, N, was frequently considered as a variable parameter resulting from the number of iterations admitted during the design process. Nevertheless, most of the studies published after 2000 used a fixed number of active elements. Such a number was typically limited to 256, as suggested by practical hardware constraints such as the scanner channel count and/or the cable complexity. In a few cases [36], [38], [51], [52], N was still considered as a variable parameter, and a fine weight was associated with each element to shape the final beam profile through the apodization.

2) Gridded Versus Ungridded Arrays: Ideally, the position of the elements of a sparse array should be set without any restriction, except for the non-overlapping condition. In this case, non-periodical patterns can be designed so that the energy of the grating lobes (i.e., the lobes originated by the spatial periodic sampling associated with the regular elements' pitch) is spread over a pedestal of average level $20 \cdot \log(1/N)$ [53]. However, such possibility requires advanced manufacturing processes (laser machining technique or micromachined ultrasound technologies, [54]). When these

processes are not available, the active elements are constrained to stay over a regular grid, like those obtainable through dicing.

3) Possible Use of Distinct TX and RX Arrays: Using distinct (sub-)arrays for TX and RX is of potential interest in sparse array design, although this involves an increased system complexity. Indeed, the effective two-way beampattern corresponds to the product of the TX and RX patterns. Therefore, thanks to an accurate design of the two layouts, the TX beampattern can have valleys at the occurrence of grating lobes in the RX beampattern and vice versa. An increased reduction of the grating lobe levels can thus be achieved.

The design of distinct TX and RX sparse arrays is often based on the so-called effective aperture or co-array function, defined as the convolution of the TX and RX apertures. According to the continuous wave (CW) far-field approximation, the effective two-way beampattern can be approximated as the Fourier transform of the effective aperture [55]–[58].

4) Simulation Complexity: The simulation of a realistic scenario for the design of a sparse array aimed at medical ultrasound imaging should consider several aspects, such as the distribution of scatterers, the speckle effect, multiple reflections and reverberations, non-linear propagation, non-homogeneous sound speed, aberrating layers, etc. All such aspects might be simulated with time-consuming approaches, such as finite-element modeling. However, considering that, in many cases, the design of a sparse array requires several iterations of the same simulation step, simplified approaches to compute the radiated fields are needed. Approximated but efficient calculation tools, such as Field II [59], k-wave [60], and FOCUS [61], have been used to model transient signals, wideband impulse responses, and the 3-D near-field spatial distribution of the acoustic field. In some studies [27], [44], [45], [58], [62], the simulation setup was further simplified by exploiting the CW far-field approximation. This approximation, although very computational-efficient, was mainly used to obtain a worst case beampattern definition in terms of secondary lobes.

As detailed in Section II-C1, the calculation complexity can also be reduced, for example, according to symmetry considerations, by limiting the simulation to one sector of the array layout [33], [50]. However, this solution limits the degrees of freedom in the position of the elements and, in turn, may worsen the rejection of grating lobes.

B. Random Methods

The design of sparse arrays is a non-deterministic, polynomial-time, hard (NP-hard) problem, in which the search for the best configuration cannot explore all possible solutions.

This limitation was highlighted by all studies addressed to the design of stochastic random sparse arrays [24]–[27]. Davidsen *et al.* [24] proposed to randomly select different subsets of elements in TX (192 elements) and RX (64 elements) out of a fully populated matrix. Specifically, they proposed a layout with mutually exclusive TX/RX subsets of elements as shown in Fig. 2. The same figure also provides an overview of different layouts addressed in the next paragraphs.

Two random array configurations were explored: one with the element density distribution being uniform for both TX and RX arrays, and a second one with a Gaussian distribution for the TX array and a uniform distribution for the RX array. Four hundred random arrays were generated and their pulse-echo beampatterns were evaluated by multi-depth wideband simulations including the spatial impulse response of individual elements. The configuration achieving the narrowest pulse-echo beamwidth was considered as the best array layout. Simulations and experiments showed that the Gaussian-uniform array was better than the uniform–uniform one. The authors highlighted that the secondary lobe pedestal was dependent on parameters such as the elements' directivity and position, the TX pulse bandwidth, and focusing. However, it is worth highlighting that testing only 400, randomly chosen, selections of elements are not sufficient if compared to the number of possible combinatorial solutions of the NP-hard problem. Indeed, the authors evidenced an important variability of the beampattern behavior across the tested random arrays. Then, as a perspective, the authors suggested that an iterative method should depend on previous trials instead of generating each time an independent configuration.

C. Optimization Methods

To overcome the inherent limitations of random approaches, several studies were dedicated to the optimization of sparse array design. The various approaches considered different degrees of freedom (linked to the parameters to be optimized), cost functions (linked to the objective of the optimization process), and strategies (typically linked to the developed algorithms).

1) Degrees of Freedom: The first degree of freedom taken into consideration was the element weight: either binary weights (i.e., enabled or disabled element) [28]–[30], [35] or full precision weights [36], [38], [51] were used. Binary weights can be used to directly select the number of active elements, N, while full precision weights enable the apodization.

To avoid the signal-to-noise ratio (SNR) loss associated with apodization, some studies preferred to consider the position of the elements as the only parameter to be optimized. A first group of researchers limited the possible positions to fixed coordinates, which could lay either on a grid [33], [63], or out-of-grid [37]. A second group allowed the elements to freely move over a plane during the optimization process [64], [65]. A hybrid solution was proposed in [39] and [40], in which the TX elements were located at fixed positions, while the RX elements were freely moved.

Other works sequentially or simultaneously optimized both the elements' positions and weights. For the very first optimized ungridded array, Boni *et al.* [50] proposed to alternate, at each iteration, the position and the weight optimization. In [33], three different optimization setups were considered: 1) optimize the positions while keeping all weights equal to 1; 2) keep a fixed pattern of the random (gridded) array and optimize the element weights; and 3) optimize both positions and weights simultaneously, see Fig. 2. The latter setup was later exploited also in [38]–[40].

The degrees of freedom are often controlled by design constraints to reduce the computation time of the optimization procedure or to satisfy some fabrication requirements.

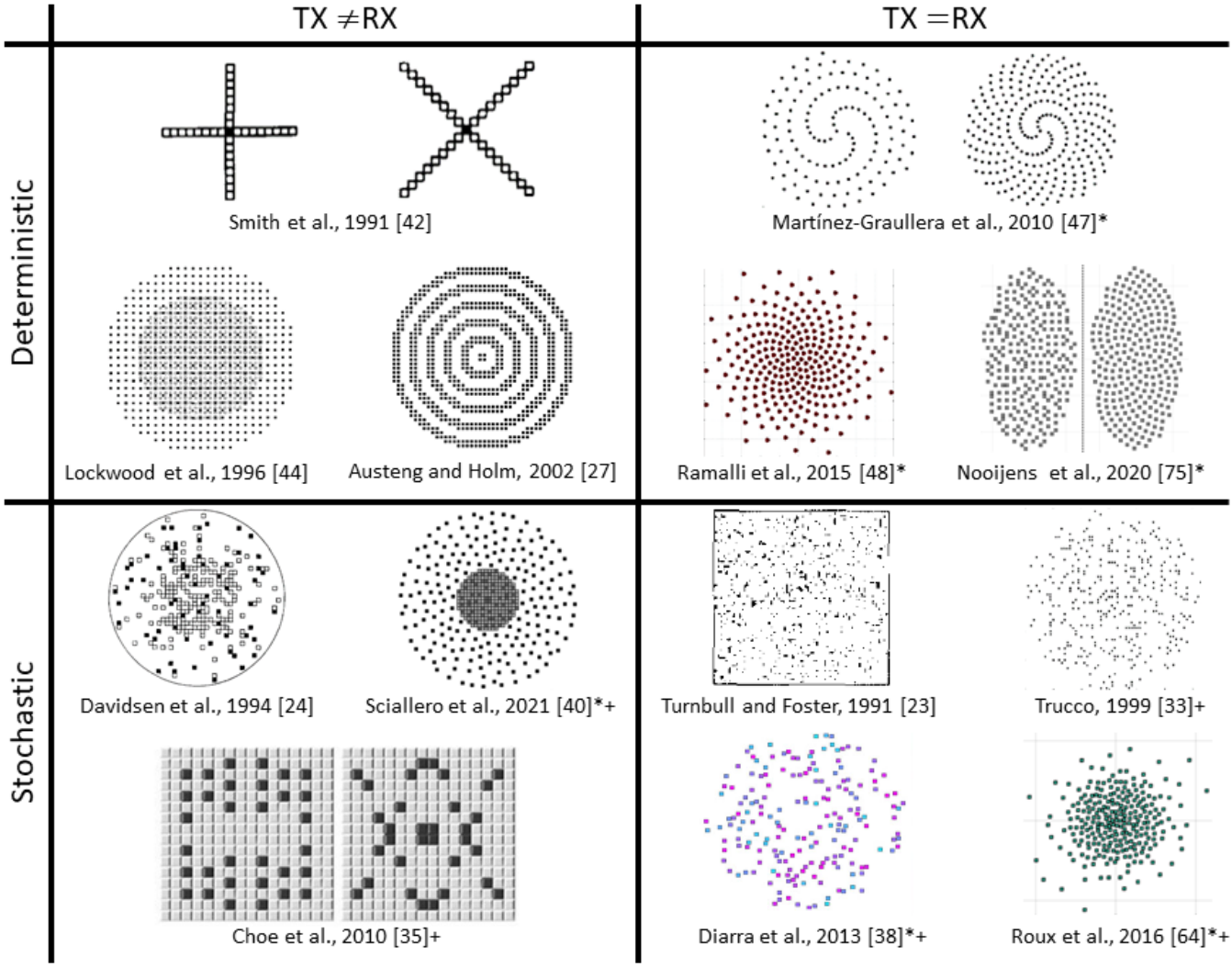

Fig. 2. Different sparse array layouts, obtained through deterministic (top row) or stochastic methods (bottom row). Either the same elements (right column) or different elements (left column) were used for transmission and reception, respectively. The arrays with elements that can be out-of-grid are indicated with a star (∗) and those obtained using an optimization procedure are indicated with a plus sign (+).

For instance, the optimization of the number of elements [33], [36], [38], [52], [51] could be addressed to match the channel number of the companion scanner. Also, specific probe footprints, with independent and/or non-overlapping TX/RX arrays, or others constraints were considered in [28]–[30], [33], [36]–[40], and [63]–[65]. Finally, the space of possible solutions was drastically reduced in [33] and [50] by imposing symmetry conditions on the array.

2) Cost Function: The optimization of a 2-D sparse array aims at achieving an optimal image quality, e.g., in terms of resolution and contrast. This goal can be addressed by minimizing the so-called cost function, i.e., the core of the optimization process. Such a function may consider several performance parameters, which are included and mixed at the author's discretion. Typically, the best 2-D array configuration is associated with the lowest value achieved by such a function. In a few cases, the criterion was rather formulated as the maximization of an objective function. This was the case of the objective function defined in [50] as the integrated sidelobe ratio (ISLR), i.e., the ratio between the energy of the main lobe and the energy of the secondary lobes in the array beam pattern (BP). In [29], [37], and [51], the maximum SLL was minimized. A distinctive feature in [29] was that the cost function integrated the BP at several steering angles.

In [39], higher costs were associated with the secondary lobes having an amplitude overcoming a reference profile. Two cost functions were considered in [30]. The first one was a weighted version of the maximum SLL, in which a secondary lobe peak close to the main lobe was associated with a higher cost than the same peak located far away. The second cost function was the error energy, which consists of the summed squared distances between the sparse array BP and the BP of a reference full array.

In [33] and [38], the cost function had one term for element thinning and one for keeping the SLL below a desired threshold, see Fig. 2. In [36], a third term was included, which aimed at limiting the amplitude range of weighting coefficients.

The first 3-D energy function [35] was defined as the ratio between the energies inside and outside of the focal volume. This computationally demanding approach required to precalculate the contribution of each element to the two-way BP (the TX elements were here different from the RX elements) so that such BP was available during the optimization process, see Fig. 2.

In [64], three different cost functions were evaluated, demonstrating the benefits of considering the BP at multiple depths. This was the first work using wideband BPs of free moving elements computed on the fly during the optimization process, see Fig. 2. In [63], the multi-depth approach was combined with a sculpting mask to define the desired BP in terms of SLL level and main lobe shape. Finally, Sciallero and Trucco [40] recently proposed a method based on wideband simulations, in which the cost function considered the BPs computed for different signal fractional bandwidths, see Fig. 2.

3) Optimization Strategy and Algorithm: The minimization of different cost functions has been addressed using various optimization strategies. The first approaches, using linear programming and eigenvector decomposition [50], [51], had their applicability limited to 1-D arrays. For a high number of elements (especially when both the element position and weight are optimized) the problem becomes intractable. Therefore, some authors proposed to exploit a GA to minimize the cost function [28]–[30], [65]. Since it is based on the principles of evolution, the GA selects the best candidate solutions among a new generation (children), obtained from the previous generation by the recombination (i.e., a stochastic mix of two parents) and/or the mutation of the operator(s) (i.e., a change limited to an individual) [28]–[30]. Other authors preferred to base their optimization on the SA algorithm [31]–[40]. SA aims at simulating the behavior of the moving atoms (here, the array elements) of a slowly cooled substance forming an ideal crystal (here, the sparse array) reaching the minimum-energy state [41]. The SA optimization procedure, as schematically described in Fig. 3, was successfully applied to the design of ultrasound arrays thanks to the following key features: 1) a solid framework is provided; 2) the finite-time convergence allows optimizing large combinatorial systems; 3) the formalism enables a straightforward parametrization of all possible array configurations; and 4) the cooling sequence, which controls the acceptance probability of uphill transitions, avoids to get stuck in local optima while converging statistically to the global optimum [41], [66], [67].

It is worth mentioning that, more recently, methods addressed to optimize the driving strategy of the sparse array elements, rather than their position, have been proposed [37], [68]. For example, a variant of the particle swarm optimization (PSO) algorithm, invented to simulate group dynamics [69], was proposed in [68]. The rationale behind this algorithm is that the macroscopic behavior of one group (e.g., the whole ultrasound array) made of multiple individuals (each active element) can be modeled through the interactions (position and velocity updates) between each individual and its neighbors. Simulations show that such an approach can generate multiple-focus patterns over the scanning range needed by focused ultrasound in the treatment of brain tumors, blood-brain barrier opening, and neuromodulation.

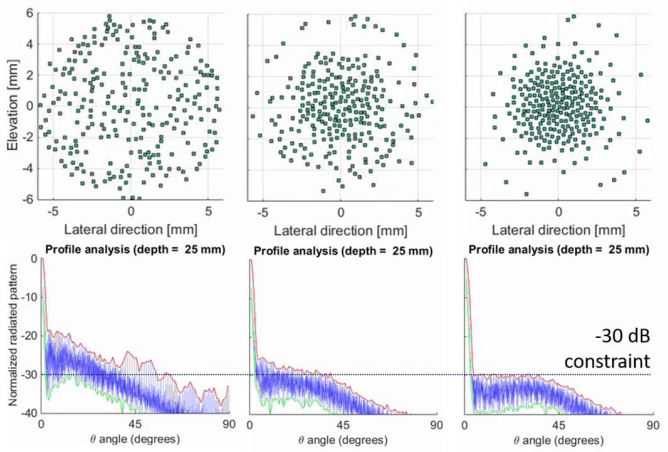

Fig. 3. Illustration of three steps (start, middle, and end) of the optimization process of a 256-element non-grid array by SA. The optimization starts from a randomly selected array layout (top-left), whose transmitted field (bottom-left) does not respect the constraints (in this example, the SLL lower than –30 dB). The optimization iterates with a decreasing acceptation rate, which implies its first half to be an exploration phase (top-middle), already improving the transmitted field (bottom-middle), while the second half of the optimization is rather a convergence phase to reach the optimal layout (top-right), which fully matches the constraints (bottom-right).

The performance of sparse arrays designed through different optimization strategies was compared in [65], while the papers [38], [63] provided an insight on the optimization robustness (i.e., the capability of obtaining a reproducible state when repeating the optimization from different seeds).

D. Deterministic Methods

To avoid the issues linked to optimization, several deterministic sparse array design approaches have been proposed in the literature.

In [42], Smith *et al.* used different subsets of active elements in TX and RX, respectively, to create two 32-element Mills crosses that were oriented at 45° to each other, see Fig. 2. Although good results were obtained (the secondary lobes were 20 dB lower than the main lobe), the authors concluded that a higher number of active elements was needed to achieve significant image quality improvements.

Austeng and Holm [27], Lockwood and Foster [43], [44], and Nikolov and Jensen [45] identified alternative sparse periodic layouts based on different TX/RX subsets of elements. In [43] and [44], Lockwood and Foster designed the sparse arrays starting from a $(0.9)\lambda/2$-sampled dense matrix. The dense matrix was undersampled with different pitches for the TX and the RX array so that the convolution of their aperture functions resulted equivalent to the aperture of a $\lambda/2$-sampled reference array. Specifically, the TX and RX array elements were selected using the vernier interpolation method with $3(0.9)\lambda/2$ and $2(0.9)\lambda/2$ spacing, respectively, see Fig. 2. Also, the elements were constrained to a circular aperture and to a radially symmetric cosine apodization function to smooth the radiation pattern. Simulations showed

that, despite a sixfold reduction of the number of the active elements (from 3117 to 517), the sparsity had a little effect on the beamforming properties of the arrays, but proportionally impacted on the signal amplitude, which was also decreased by the apodization.

A thorough study on 2-D vernier arrays [70] showed that they provide lower average and peak secondary lobes compared to sparse random arrays with the same number of elements and aperture size. The study derived a set of design curves to predict the number of elements, apodization window, and element sparsity needed to achieve the desired beamwidth and maximum SLL. However, in [71], Yen *et al.* showed that when 2-D vernier arrays are used to reconstruct wide, parallelepipedal regions of interest, the element sparsity must be further increased with a consequent boost of the off-axis grating lobes level. In addition, since the elements of 2-D vernier arrays are selected along the two lateral directions, the vernier nature along the diagonal directions is broken. To solve this issue, in [45], an additional element was inserted between two RX elements in the diagonal direction, yielding a further reduction of the SLL by about 9 dB.

Different sparse periodic layouts were investigated in [27]. The design, aimed at achieving a TX response with zeros at the occurrence of grating lobes in the RX response and vice versa, was based on the far-field, CW approximation of the BP radiated from omnidirectional point transducers. The layouts were classified as: 1) regular sparse periodic layouts, characterized by either symmetric or asymmetric periodicity along the main axes and 2) radially sparse periodic layouts, whose periodicity was defined along the radius and looked like multiple and concentric ring-shaped arrays, see Fig. 2. Also, two semi-random approaches for finding non-overlapping TX and RX layouts were proposed. Both were based on the random binned array idea [72] and aimed at maximizing the average inter-element spacing by selecting bins either on rectangular regions or along concentric rays. The sparse arrays were derived from an initial 48 $\times$ 48-element dense array (center frequency = 3 MHz, pitch = 308 μm) whose corner elements were eliminated to obtain a circular array footprint of 1804 elements. The performance of fourteen sparse layouts was compared showing that a trade-off among the number of elements, sensitivity, beamwidth, and ISLR can be found to assure high-quality pulse-echo responses.

Following a different approach, Karamann *et al.* [62] studied the spatial frequency content of the co-array (or the effective aperture) function. The authors aimed at the design of co-array functions that captured all the spatial frequency contents with a minimum number of TX/RX element pairs, i.e., by eliminating the redundant pairs of elements that contributed to the same spatial frequency. The method was initially tested with a 32 $\times$ 32-element dense array (center frequency = 5 MHz, pitch = 150 μm) for endoscopic applications. Four TX/RX combinations of sparse arrays, which included x-shaped, plus-shaped, boundary-rows, and boundary-columns arrays were considered. For each configuration, the performance was evaluated in terms of the number of TX/RX elements, the number of TX/RX active channels, SNR, point spread function, and frame rate, when implementing volumetric scanning based on fan-beams. Compared to a full array, the proposed sparse arrays suffered from low TX acoustic power and SNR (–30/40 dB).

A preliminary study [46] proposed to place the elements of a 255-element array (128 in TX and 127 in RX) along an exponential spiral. Its superior performance, in terms of SLL, compared to random and periodic arrays was confirmed by wideband simulations.

Fermat spiral has been recently proposed as an ideal reference for the design of deterministic sparse arrays using the same elements in TX and RX [47], [48]. For a given aperture size, this spiral allows defining the position of each element by only two parameters: the divergence angle and the total number of elements. Moreover, the inherent rotational symmetry is ideal for volumetric imaging. In [47], 60λ, 50λ, and 40λ wide apertures were simulated with 256 elements at a minimum interelement distance greater than λ. For each spiral array, two configurations were tested: one used the same TX/RX aperture, see Fig. 2, while the other one used half (128) of the elements in TX and the remaining elements in RX. For both configurations, several layouts were simulated by finely varying the convergence angle; then, the related two-way beampatterns were computed for both CW and wideband (60%) simulations to determine the best performing array in terms of SLL, resolution, and main-to-secondary lobe energy ratio. The article concluded that both configurations offer similar lateral resolution, but secondary lobes are lower when the same 256-element array is used in both TX and RX.

In [48], 256-element arrays based on Fermat's spiral with a divergence angle equal to the golden angle were proposed. Such an angle (222.49°) generates the so-called sunflower arrays, i.e., arrays having elements distributed with constant spatial density. Since this distribution produces large grating lobe regions, the method originally proposed in [73] and [74] for antenna arrays was adapted to taper the density of elements, see Fig. 2. Such an approach allows increasing the probe sensitivity while simplifying the transmit section of the system, which does not need element-dependent amplitude control. Wideband simulations of 3-D one-way fields were computed for 105 array configurations by modifying the aperture diameter (80λ, 60λ, and 40λ), the element size (0.5λ, 0.7λ, 1.0λ, 1.2λ, and 1.5λ), and the density tapering windows. The performance of the arrays was evaluated in terms of grating lobe levels, secondary-to-main lobe energy ratio, sensitivity, resolution, and depth of field for 25 different steering angles. The results were provided as a reference guide for the design of spiral arrays in different application fields.

In [75], Fermat's spiral was considered for the development of arrays dedicated to volumetric transperineal ultrasound imaging (TPUS) of the prostate. Since the circular footprint of Fermat's spiral did not fit the TPUS asymmetric acoustic window (3 $\times$ 5 cm^2), 256-element ellipsoidal arrays were designed. Different layouts were simulated by varying the element size, the center frequency, the minor semi-axis length, and the aspect ratio of the ellipse. The layouts were compared in terms of steering capability, energy output, resolution, and contrast-to-noise ratio, to select the most suitable one for production by dicing, see Fig. 2.

A method to further increase the sparsity of spiral arrays was recently proposed in [49]. The authors observed that the grating lobes generated by a sunflower array form a ring around the main lobe, whose angular position depends on the average interelement distance. Different, partially overlapped, TX/RX apertures were designed with elements selected by respecting the vernier interpolation along with the angular position. The average interelement distance of TX and RX layouts turned out to be different and the grating lobe ring of the TX array fell on the nulls of the radiation pattern of the RX array and vice versa.

III. Review of Experimental Work

A. Implementation of Piezoelectric Arrays

1) Early Sparse Array Implementations: To the best of our knowledge, the first experimental evaluation of the performance obtained by a 2-D sparse array was done in [42]. Smith *et al.* [42] constructed two gridded arrays consisting of 20×20 elements each, operating at 1.0 MHz (pitch = 1 mm) and 2.3 MHz (pitch = 0.6 mm), respectively. Since the available imaging system included only 32 TX and 32 RX channels, the arrays were tested connecting such channels to two Mills crosses, each of 32 elements. The RX cross was obtained by selecting elements oriented at 45° to the elements of the TX cross. For the 1.0 MHz array, the measurements demonstrated that the pulse-echo point spread responses well matched the simulations, showing –6 dB beamwidths of 5.6°, and a first secondary lobe at 15 dB below the main lobe. The sparse array, originally developed and implemented at Duke University, was expanded and further improved in subsequent studies [76].

An ultrasparse wideband array with 3.75 MHz center frequency, consisting of 4×4 elements placed on a regular grid with 15.5λ spacing, was synthetically implemented in [26]. The experimental setup was based on a hemispherical transmitting (point) source, and a receiving hydrophone, which was moved on step-by-step over the plane of interest. The overall beampatterns, calculated by hypothesizing a linear ultrasound propagation and exploiting the superposition principle, showed good agreement with simulations in terms of SLLs (<12.5 dB). However, this approach was only tested in water, and no images were provided.

The work by Austeng and Holm [77], describes the experimental validation of sparse arrays designed according to the methods illustrated in [27]. Data were obtained through a 50×50-element 2-D array, with 0.6λ pitch and 3 MHz TX frequency. Since 100 TX and 100 RX elements could be simultaneously connected to the scanner, manual switching of 100 elements was performed 625 times, to collect data from 25×25 possible combinations of 100-element TX/RX groups.

The array was connected to a GE Vingmed Ultrasound System Five scanner using 1-cycle sinusoidal bursts as excitation signals. Echo data from a phantom including nylon wires at different positions were acquired with a synthetic aperture scan sequence. Acquired data were offline dynamically beamformed in both TX and RX to form synthetic aperture 3-D volume images. Although the level of the artifact was higher than that expected from simulations, the experiments showed that the sparse arrays, using less than 50% of the TX elements and down to less than 30% of the RX elements, were able to produce good quality wire phantom images with a 60-dB dynamic range.

2) Sparse Arrays Derived From the Vermon Matrix Probe: Vermon S.A., Tours, France, recently made available two piezoelectric matrix probes operating at 3.5 and 7.5 MHz central frequency, respectively. Both arrays consist of 32 by 35 elements (300 μm pitch, bandwidth > 50%) but, since every ninth row is not connected, the total number of addressable elements results in 1024.

Such probes have been mainly used together with high-element count research scanners [13]–[15], [78] to develop innovative 3-D applications. They have also been used to test different sparse array configurations obtained by selecting corresponding groups of elements out of the original 1024-element array. In all these cases, of course, the results are influenced by fabrication constraints such as the pitch, element size, and unconnected element rows.

A first (software) selection was proposed in [63]. Here, four Vantage-256 research scanners (Verasonics, Inc., Kirkland, WA, USA), were synchronized [14] to drive the 1024-element, 3.5 MHz, Vermon matrix probe. The channels of the scanners were programed to activate at the same time only 256 elements, selected to reproduce the optimal array configuration described in [63] (the so-called opti256 array obtained through the SA algorithm, see Fig. 4 left). As reported in Section III-C, this approach allowed comparing the experimental results obtained by the sparse array with those obtained by the reference full array.

A hardware selection approach was used in [79]–[81]. Here, the layout design was based on an ungridded, 10.4-mm-wide spiral with 256 seeds, whose density tapering was modulated according to a 50%-Tukey window [48], see Fig. 4 center. A first (main) layout was obtained by selecting the elements closest to the ideal positions of the spiral seeds (see Fig. 4 right). A second sparse layout was obtained with the same strategy applied to another ideal spiral, which was rotated by a golden angle relative to the first one. Of course, the elements already assigned to the first layout were excluded from the second one. The two sparse layouts were connected to distinct connectors so that either two independent 256-element sparse arrays or a single 512-element array could be used. Section III-C reports different applications of this dual sparse array probe.

All sparse array probes derived from the Vermon probe have demonstrated good performance in focused B-mode imaging [63], [80]–[82], achieving comparable lateral resolution and slightly worse contrast compared to the full array. However, as expected, the reduction of the number of elements had a significant impact on the SNR. This aspect is discussed in detail in Section IV.

3) PZT-on-PCB Spirals: In [83] and [84], the development of a spiral array, based on a lead zirconate titanate-on-printed circuit board (PZT-on-PCB) technology, was presented. Here, starting from the geometrical definition of a density tapered spiral pattern [48] with 256 active elements, a grid snapping

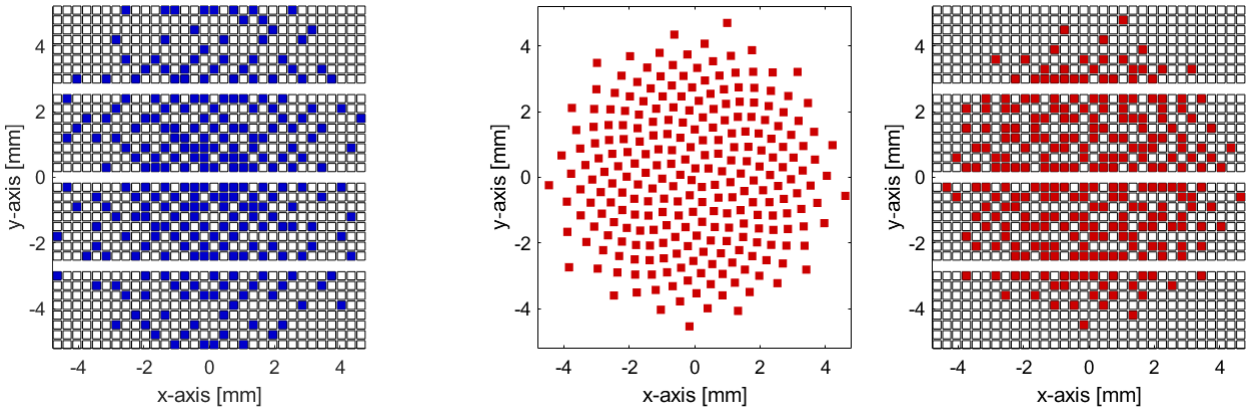

Fig. 4. Layouts of the sparse arrays implemented on the Vermon matrix probe. The layout on the left was obtained through SA optimization and software elements selection [63]. The layout on the right was obtained through hardware selection of the elements closest to the ideal positions of the sunflower seeds (center) [79]–[81].

was operated to adapt the actual elements' position to a 220 × 220 μm grid, which was then used for transducer dicing. The elements selected from the full grid were connected to the back-side PCB by gold balls and conductive epoxy. Considering the relatively high impedance of each probe element, the cable attenuation was prevented by associating the array elements with an equal number of in-probe preamplifiers (MAX4805, MAXIM Integrated, San Jose, CA, USA) [85]. The array was designed for 5.5 MHz operating frequency and the prototype, having a total aperture of 16 mm, showed a transmit SLL of –18.2 dB when steering at 16° both in azimuth and elevation. The one-way lateral resolution, when focusing at 20 mm depth, was 1 mm. The transmit/receive –6 dB bandwidth was narrower than expected (1.8 MHz instead of 2.8 MHz), likely due to the poor acoustical performance of the FR4 PCB substrate, which also acts as the acoustical backing layer.

4) Logarithmic Spiral Array: In [86], a log spiral array pattern was selected among three aperiodic sparse array configurations with 2 MHz center frequency and 30 mm aperture, aimed at transcranial Doppler applications. Simulations showed that such a pattern yields the best trade-off between optimal peak SLL and ISLR values. A piezoceramic fiber-based composite element composite array transducer (CECAT) and a conventional 1–3 composite (C1–3) array were manufactured and their performance compared. In both cases, the arrays consisted of 70 circular elements, each with a 0.95 mm radius. The CECAT structure exhibited a reduced (10 dB lower) crosstalk between neighboring array elements, and wider fractional bandwidth (47% versus 31%). However, according to pulse-echo experimental measurements, the sensitivity of the C1–3 device was ∼50% higher.

B. CMUT Implementations

A 128-element CMUT sparse array [87] was fabricated by direct wafer-bonding, with a special procedure [88] based on consecutive thermal oxidation steps, see Fig. 5(A) and (B). Each element was composed of a 3 × 3 array of 24 μm elementary cells. The location of each element was optimized

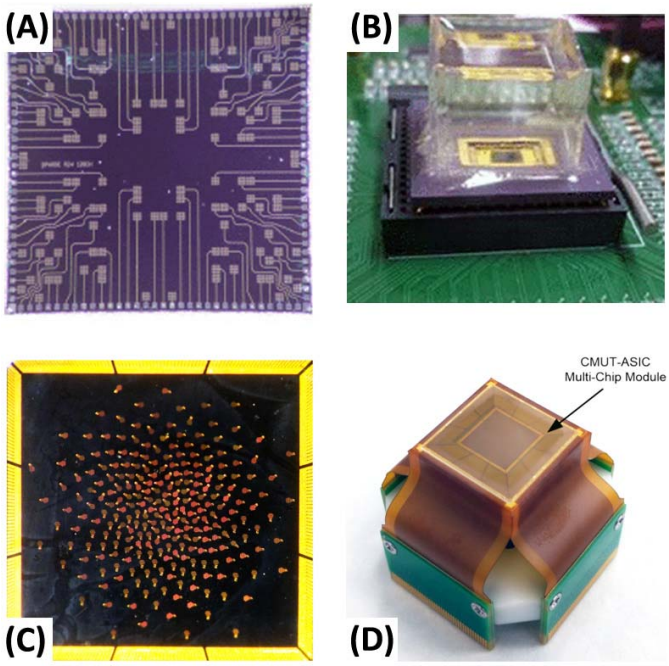

Fig. 5. (A) 128-element CMUT sparse array covering a surface of 5.76 × 5.76 mm^2 [87]. (B) Device, wire-bonded on the chip carrier with a packaged oil tank, was connected to the circuit by a zero insertion force (ZIF)-socket for 3-D imaging test. *2017 IEEE. Reprinted, with permission, from* [87]. (C) 256-element density tapered CMUT spiral array [89]. The CMUT elements are spread over a surface of 10.2 × 10.4 mm^2. (D) Chip was interconnected to an AFE ASIC through a 3-D packaging method, and packed to the probe head. *© 2018 IEEE. Reprinted, with permission, from* [89].

by a SA method over an area of 5.76 × 5.76 mm^2, corresponding to that covered by a full-gridded array of 1024 elements. The elements showed a center frequency of 3 MHz, and the preliminary B-mode and C-mode images presented a –3 dB lateral resolution of 2 mm (4.73λ) and a –3 dB axial resolution of 300 μm (0.71λ).

In [89], a 256-element CMUT spiral array was fabricated using the reverse fabrication packaging procedure [90]. The array geometry, shown in Fig. 5(C) and (D), was that of a

density tapered spiral [48], designed for operation at a center frequency of 7 MHz with an aperture diameter of 10 mm. Each element was composed of 19 CMUT membranes arranged in a hexagonal pattern, with a total element size of 220 μm.

The electrical impedance of CMUT elements is strictly related to their capacitance, which is in the order of hundreds of femtofarad. This implies an impedance of several kΩ, which cannot be managed by in-probe preamplifiers, due to the added stray capacitance between the CMUT head and the in-probe amplifier PCB. This encouraged the integration of a 256-channel analog front end (AFE) ASIC. The AFE was co-designed with the array and interconnected to the latter through an innovative acoustically optimized 3-D packaging method [91]. The resulting multi-chip module was electro-mechanically and acoustically characterized. The one-way beampatterns showed an SLL of –23.2 dB at a 27° steering angle. The elements showed a transmit bandwidth of 7.4 MHz.

In [92], a dual-ring array for forward-looking imaging was fabricated in CMUT technology. Ring-shaped arrays are intrinsically sparse arrays, due to the hollow space at the center of the aperture needed for their integration with a catheter in intracardiac or intravascular applications [93], [94]. The CMUT arrays described in [92] had 56 TX (outer ring) and 48 RX (inner ring) elements, with 1.31 and 1.13 mm center diameters, respectively. Each element, roughly 70 μm × 70 μm wide, consisted of four individual membranes and operated at a center frequency of 12 MHz.

The experimental test was based on the method proposed in [37]. Specifically, the authors found, through SA, the optimum firing set from different TX and RX elements to produce wideband point spread function with low side lobes. They showed that, compared to the full firing set, the optimal one achieved similar lateral and contrast resolution with less than 1/5 of the firings.

C. Applications

1) HFR and Tri-Plane Cardiac Imaging: The work by Roux *et al.* [82] reported on high frame rate (HFR) volumetric acquisitions based on the transmission of diverging waves (DWs) from the aforementioned opti256 sparse array. Twenty-five low-quality volumes were reconstructed by transmitting DWs from 5 × 5 virtual sources, which were distributed over a sphere with a 25 mm radius from the center of the array (field of view of ±25.4°). The final compounded volume was obtained by averaging the 25 low-quality volumes (each from 15 to 90 mm depth) to enhance contrast and resolution. The experiments demonstrated a potential rate of 90 volumes/s (pulse repetition frequency (PRF) = 2.2 kHz). The sample images in Fig. 6, obtained with the reference 1024-element array and with the opti256 array, respectively, highlight a limited difference of quality, in this case.

The double spiral probe described in Section III-A2 was used in combination with two ULA-OP 256 open scanners [95] for real-time HFR tri-plane echocardiography [80]. Here, five TX–RX combinations of the two 256-element sparse arrays were tested. Tri-plane imaging was implemented by scanning three sectors, positioned at rotational angles of 0°, 45°, and 90°, corresponding to the approximate position of the apical 2-, 3-, and 4-chamber views, respectively. The imaging performance was assessed on a thick-walled univentricular phantom [96], by implementing four scan sequences based on conventional focused transmission, focused multi-line transmission, diverging single-plane transmission, and diverging multi-plane transmission, respectively. The authors concluded that sparse arrays are effective for the implementation of HFR tri-plane imaging although some loss in image quality and sensitivity is unavoidable. Moreover, multiline transmission by sparse arrays allows achieving the same temporal resolution currently used in clinical 2-D echocardiography, while the transmission of planar DWs boosts the frame rate up to 250 Hz, enabling the real-time functional analysis of the heart.

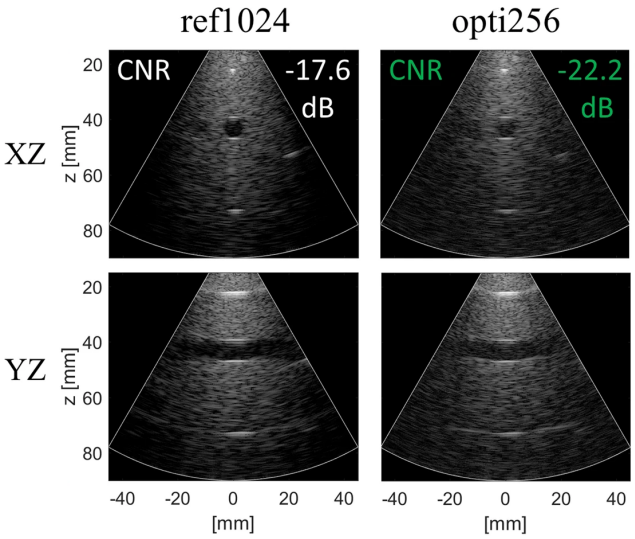

Fig. 6. Comparison between reference full array (ref1024) and optimal sparse array (opti256) images from the azimuth (*XZ*) and elevation (*YZ*) planes, respectively. 3-D DWs were used in TX (dynamic range: 60 dB). ©.

2) Blood Flow Detection: The effect of element sparsity on blood flow imaging was first experimentally tested in [97]. The spectral Doppler performance of the 256-elements sparse layout optimized by SA (opti256, see Section III-A2), was compared to that of the 1024-element Vermon probe. This was possible through the software element selection described in Section III-A2.

Flow phantom experiments showed that the sparsity of elements did not significantly affect the shape nor the mean frequency of pulsed-wave Doppler spectra. The missing rows of the Vermon probe generated spectral secondary lobes, whose level was comparable to the noise level and therefore were barely visible. The major concerns were related to the poorer SNR of the sparse array, which might limit the *in vivo* Doppler investigation of deep vessels.

This problem was faced in [81] by implementing real-time coded TX and matched filtering in RX on the ULA-OP 256 scanner, which was connected to the 256 elements corresponding to the main spiral-based Vermon probe layout (see Section III-A2). The article showed that the TX of 5 μs long

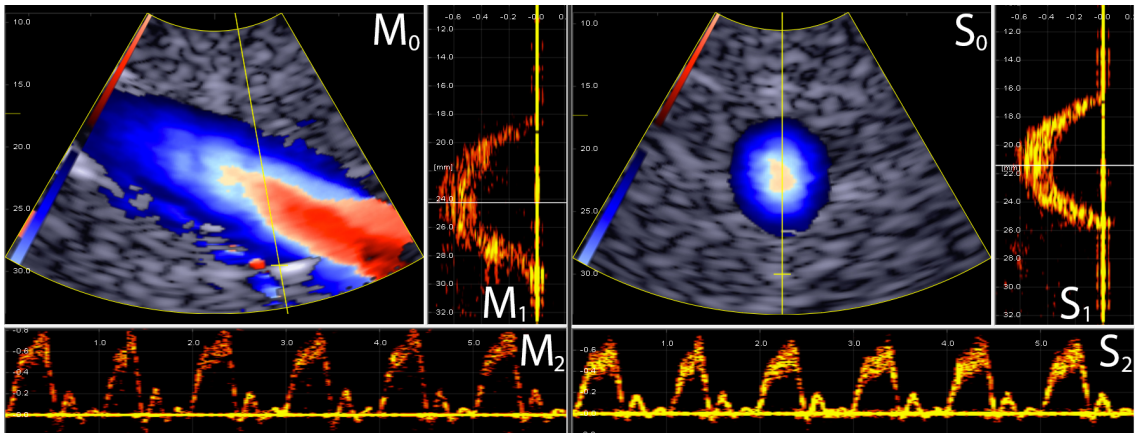

Fig. 7. Screenshot of the graphical user interface of the ULA-OP 256 during real-time HFR bi-plane imaging based on two sparse spiral arrays. The left and right display windows, each associated with one scanner, were split in three different panels showing B-mode and color flow images (M_0, S_0), multigate spectral Doppler images (M_1, S_1), and spectrograms (M_2, S_2). *© 2021 Mazierli et al. under Creative Commons license. Reprinted from* [14].

linear chirps, each spanning a band of 2.7 around 3.7 MHz, allowed gaining 11.4 dB of SNR when compared to a short sine burst TX. *In vivo* flow profiles were detected along non-coplanar investigation lines that were easily positioned through bi-plane B-mode imaging.

In [98], the same spiral probe layout was used to experimentally validate a novel high frame rate 3-D vector flow imaging method. The probe here transmitted unsteered plane waves at 3.7 MHz. Post-processing of acquired raw echo data produced encouraging 3-D vector velocity measurements, although the small probe aperture (~10 mm) limited the size of the region of interest (~10 × 10 mm^2).

The double spiral probe described in Section III-A2 was also recently used together with two synchronous ULA-OP 256 scanners in real-time HFR imaging experiments [14]. In TX, all 512 active elements were excited to simultaneously insonify two perpendicular planes by planar DWs. In RX, the echoes collected from each of the two sparse arrays were synchronously and independently processed by the two scanners. In real-time, HFR (1300 frames/s) B-mode images were obtained together with 40 color flow maps/s and 40 multigate spectral-Doppler images/s (see Fig. 7).

In [99], the feasibility of real-time imaging the brain through a sparse array, selected out of a 40 × 40-element matrix array, was demonstrated. In subsequent studies [100]–[102], starting from an 80 × 80-element gridded probe with 2.5 MHz center frequency, the authors selected different sets of TX and RX elements based on sparse periodic vernier patterns, to synthesize the arrays for single and multi-transducer volumetric 3-D transcranial Doppler imaging. The number of TX/RX elements was 440/256 for single transducer applications and 256/128 for dual transducer applications. The implemented systems, accessing from the temporal and sub-occipital transcranial windows, were able to produce real-time 3-D ultrasound images of the cerebral vasculature. The overall –6 dB beamwidth was 5.5 mm at 70 mm depth, with –60 dB grating lobe level.

3) Microbubbles/Super-Resolution Imaging: Sparse arrays can be effective in super-resolution techniques using ultralow-density contrast agents for micro-vessels identification.

In [103], Definity[1] microbubbles (Lantheus Medical Imaging, North Billerica, MA, USA) within a spiral tube phantom, having an internal diameter of 255 μm, were mapped through an *ex vivo* human skull. In TX, a pseudorandom distribution of 128 elements, selected out of a 30-cm-diameter, 1372-element, hemispherical transcranial therapy array [104], was driven by a 128-channel research scanner (Verasonics, Inc., Redmond, WA, USA). In RX, 128 piezo-ceramic disk elements (Del Piezo Specialties, LLC., West Palm Beach, FL, USA), sparsely distributed in a pseudorandom configuration over a hemisphere cap, were connected to a 128-channel receiver (SonixDAQ, Ultrasonix, Richmond, BC, Canada). The narrowband receiver elements were tuned to two times the driving frequency to achieve good sensitivity to the harmonic bubble activity. Super-resolved images were obtained after applying phase and amplitude correction techniques to compensate for the aberrating effects of the skull bone. The positions of individual bubbles were finally estimated beyond the diffraction limit of ultrasound.

In [79], the 256-element sparse arrays described in Section III-A2 were connected to two synchronized ULA-OP 256 research scanners [14]. All 512 elements transmitted plane waves, but the data acquired from each array were separately beamformed and post-processed. First, a singular value decomposition filter extracted the microbubble signal. The acoustic sub-aperture processing (ASAP) method [105] was then applied to the filtered signals. Finally, after summing and thresholding the two volume-sets, super-localization of microbubble was performed with an 18 μm localization precision. The system thus allowed super-resolving two 200 μm tubes (smaller than one-half of the imaging wavelength of 404 μm), and flow velocities within these tubes were calculated, as shown in Fig. 8 [106]. It is worth noting that the use, in reception, of two 256-element sparse arrays rather than a single 512-element array, promoted an SNR increase up to 5.1 dB. This is an effect of the ASAP method that benefits from the fact that a noisy signal resembling a microbubble echo is unlikely to occur

[1] Trademarked.

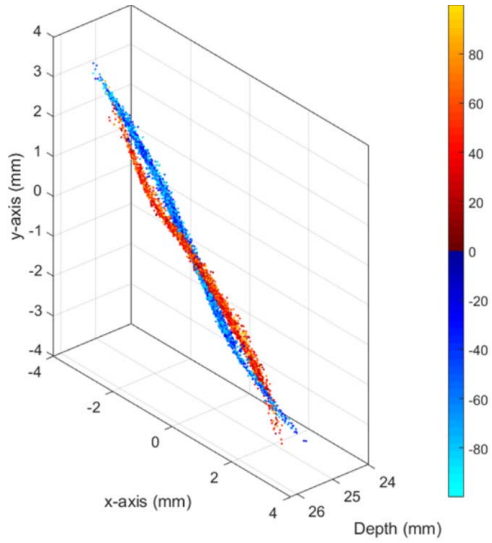

Fig. 8. Three-dimensional super-resolved velocity maps of two 200-μm diameter cellulose tubes. © *2020 IEEE. Reprinted, with permission, from* [106].

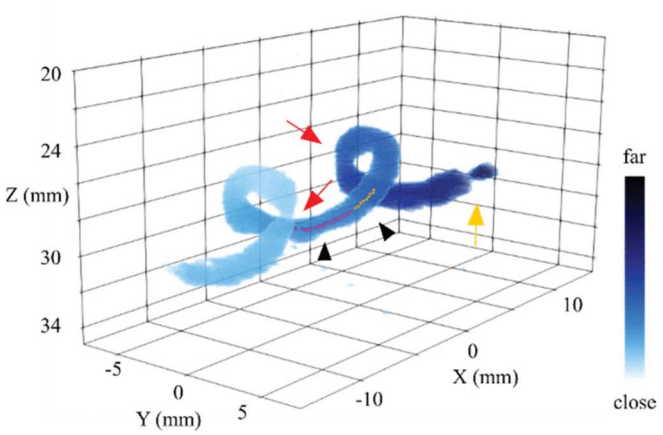

Fig. 9. Helicoidal microvessel volume rendering obtained by HFR imaging of microbubbles through the piezoelectric spiral array presented in [107]. The color map corresponds to distance to the spatial location ($x = -15$, $y = 0$, $z = 20$ mm). The black arrowheads point two sample tracks of super-localized microbubble positions. The yellow arrow indicates an artifact caused by nonoverlapping transmit beams. The red arrows indicate locations where the vessel diameter appears slightly underestimated. © *2021 Wei et al. under Creative Commons license. Reprinted from* [107].

simultaneously on the beamformed volumes from different arrays/systems.

In [107], the piezoelectric spiral array described in Section III-A3 was used for HFR volumetric imaging of microbubbles. A study was conducted to optimize the quality of transmitted DWs, producing wavefronts with limited non-uniformity. In reception, spatial coherence beamforming was used to reduce the clutter levels. The experiments demonstrated that by combining a spatial coherence beamformer with sparse-array specific TX schemes, high-quality volumetric contrast images can be obtained (see Fig. 9), and individual microbubbles can be visualized.

4) Photoacoustic Imaging: In photoacoustic (PA) imaging [108], [109], short electromagnetic (e.g., microwave or laser) pulses are used to irradiate a biological tissue. The thermoacoustic effect results in the emission of ultrasound signals that can be detected by wide-band ultrasonic transducers. The goal of PA imaging is to produce an image that represents an estimate of the spatially variable electromagnetic absorption properties of the tissue.

Initial PA experiments used linear arrays to produce 2-D images. To capture the true 3-D nature of the objects, this modality has naturally evolved toward 3-D PA imaging, which must be based on a matrix of elements. Even in this case, a strong motivation to reduce the number of RX elements has pushed toward the use of sparse arrays. In [110] an annular array was designed to permit the laser illumination of the object through the center of the probe. The array was a 30-mm-diameter ring and consisted of only 14 polyvinylidene fluoride (PVDF) film detectors. Each detector had a circular shape having a 3-mm diameter. To properly reconstruct the object, with such a low spatial sampling of the received ultrasound field, an iterative image reconstruction algorithm, originally developed in [111], was used. 3-D images of point sources and a line source were obtained with good contrast and accurate volume localization. The resolution was estimated to be 1–2 mm perpendicular to the detection plane and 2–3 mm in the detection plane.

This initial study opened the path to the investigation of image reconstructions algorithms. For instance, several groups followed the compressed sampling framework which enables (under certain conditions) high-quality image recovery despite acquiring only part of the data usually needed [112].

The need of using an adequate number of transducers (i.e., not excessively low), is testified by the work of Roumeliotis *et al.* [113]–[115], who initially developed a setup based on 15 transducers, but later extended such number to 30 and then to 60. Such elements were distributed on a hemispherical geometry. More recently, the development and characterization of a low-cost, fast PA imaging system optimized to achieve a temporal resolution of 1.5 s with a 240 μm spatial resolution, suitable for small animal imaging, has been described [116]. Here, 16 sparse elements are associated with a Q-switched NdYAG laser. Other groups have recently investigated similar approaches [117]–[119].

It is worth noting that in all these studies, differently from the case of ultrasound imaging, no efforts were done to optimize the array configuration.

5) Therapeutic: In general, therapeutic ultrasound produces thermal or mechanical effects by delivering high energy to the tissue of interest [120]. First systems were based on large single elements that needed to be translated over the region of interest to treat a full organ or lesion. As for the domain of imaging, therapeutic ultrasound has benefited from the flexibility offered by phased arrays to quickly modify the direction and shape of the beam [121]. However, when the steering is involved, the spatial sampling of the phased arrays must be very fine ($<\lambda/2$), which leads to a high channel and element count to produce a sufficient biological effect over large active surfaces.

This has motivated the therapy community to explore sparse arrays already back in 1996 [122]. In this study, an array of 108 elements with 8 mm diameter and 2.1 MHz central

frequency was first simulated, then implemented, and experimentally tested for ultrasound surgery. The system driving the probe was connected only to 64 elements, which were initially positioned regularly over the probe footprint. In such a configuration, the beampattern exhibited important grating lobes due to the large inter-element spacing. In the same study, a random sparse array configuration was also tested, demonstrating the ability to significantly modify the grating lobe patterns.

The potential of random distributions of elements for ultrasound surgery was further investigated in [123] through simulations, while in [124] two deterministic (hexagonal and annular) and one quasi-random layout were investigated for transcranial application. The quasi-random configuration exhibited lower grating lobes in the near field, which is important to reduce heating in the skull bone. The study proposed a few years later [125], highlighted the drawbacks related to the use of sparse arrays: significantly more power is required to perform equivalent ablation and, even if grating lobes are reduced, additional energy is delivered elsewhere in the medium. This has, however, not discouraged the research in this field. The combination of sparse arrays with different frequencies and focusing capabilities was proposed in [126] and [127]. Interestingly, the corresponding prototypes were also used for passive imaging to monitor the therapeutic procedure by induced cavitation [127].

To control the shape of the pressure field in the pre-focal zone, Ramaekers *et al.* [128] has proposed to adopt a spiral distribution of the elements. In [129], the performance of a 16-arms spiral layout was improved by increasing the filling factor of the probe footprint. This is possible provided the elements can have any kind of shape and not only rings or rectangles as in most other studies.

IV. Drawbacks, Technological Issues, and Countermeasures

Two different types of 2-D arrays characterized by a limited number of elements are currently used in combination with open scanners to perform 3-D experimental tests: the RCA and the sparse arrays. Compared to the latter ones, RCA arrays generally offer a lower channel count and enable higher SNRs and penetration depth. However, the volumetric images produced by RCA arrays suffer from edge effects caused by the long elements [130], [131]. Furthermore, such arrays have limited 3-D steering capabilities since they can only focus in one direction at a time, e.g., lateral in transmission and elevation in reception. Finally, without the integration of a diverging lens, their field-of-view is limited to the forward-looking rectilinear volume region in front of the transducer [20], [132], [133]. In contrast, sparse arrays can be designed to cover the same aperture and field-of-view covered by reference dense arrays, and approaches such as DW imaging can be profitably used [80], [82].

Although the resolution and field-of-view of a sparse array can be made similar to those of a reference dense array, the imaging quality is in general significantly different. The most obvious limitation of sparse arrays consists in the unavoidable beam degradation associated with a higher lobes pedestal. In general, such performance worsening depends on the ratio between the number of elements of the sparse and the reference dense array [24], [26], [48], [53]. For example, in [48], the SLL obtained with a 256-element sparse array was shown 20 dB worse than that produced by a 6684-element dense array covering the same 60λ-aperture with elements having the same $\lambda/2$ size. On the other hand, in the experimental work [77], [82], the ratio of the active elements was between 0.25 and 0.5, i.e., relatively high. Correspondingly, the beam degradation was moderate and similar resolution and contrast, in focused TX mode, were obtained. In the experiments based on the Vermon probe [82], however, such a small difference could also be partly attributed to the non-ideal density of the probe, in which a few lines of elements are missing.

Of course, there are still margins of improvement in the two-way beams achievable by sparse arrays, as testified by the large number of recent studies looking for an optimal layout definition. Among these studies, the novel adaptation of sunflower spiral layouts [49], the application of fractal geometries [57], and the mixed-use of TX dense and RX sparse arrays [40] seem to be the most promising ones.

A specific technological limitation of most 2-D arrays is related to their small active aperture, which limits the field of view and forces the use of phased imaging sequences. Moreover, their small element dimensions (typically one- or half-wavelength wide in both x- and y-directions), especially in sparse arrays, yield low sensitivity. A possible increase of the element size improves the sensitivity, but this comes at the expense of the directivity [56]. In [134], a random distribution of element sizes was proposed. Simulations showed that, compared to the array with single-size elements, the grating lobes were reduced by 1 and 7 dB, in lateral and elevation directions respectively, while the array active surface increase led to a $\approx$13 dB better sensitivity. Of course, such an approach adds another degree of freedom to the optimization procedure, thus increasing the design and implementation complexity.

In general, the reduction of the number of active elements, typical of 2-D sparse arrays, can make critical the attainable SNR. Compared to a reference dense array, every time the number of (sparse) active elements is halved, the pressure amplitudes of the associated beams are halved, too. Assuming a linear regime, in TX, the signal loss is about 6 dB/octave, i.e., 6 dB each time the number of elements is halved. In RX, thanks to beamforming, the signals received by the different elements constructively interfere, but noise, being uncorrelated, does not. The SNR loss due to element halving, in RX, is therefore only 3 dB/octave. Overall, the total, TX/RX, SNR loss is 9 dB/octave, as experimentally confirmed in [14], [82], and [97].

The inherent poor sensitivity of 2-D sparse arrays must be faced by minimizing any other possible cause of SNR reduction. Additional, undesired, element reductions, such as those originated by the so-called missing (dead) elements, must be limited as much as possible by taking special care of the probe fabrication and interconnections. A further aspect to consider is that the small array elements inherently have a high electrical impedance. Their direct interconnection to a probe cable, typically characterized by high capacitance,

may dramatically reduce the delivered voltage, resulting in poor SNRs. In [85] and [135], the use of discrete in-probe preamplifiers in a sparse PZT probe was shown valuable to increase the SNR, on average, by 16 dB. Recent advancements in preamplifier technology allow limiting the in-probe power consumption even using off-the-shelf components. For example, the MAX14822 (Maxim Integrated, San Jose, CA, USA) amplifiers draw 1.2 mW per active channel, thus producing a limited overall heat when a few hundred channels are used. In the case of CMUT probes, the element capacitance may be so small that special charge pump amplifiers might be needed, and in this case, the optimal solution would be integrating them as close as possible to the array elements in an ASIC.

In addition, advanced methods, originally developed for full arrays, could be implemented to counteract specific limitations of sparse arrays. For example, coded imaging [136]–[139], developed to improve the SNR, can also be exploited to contrast the poor sensitivity of sparse array probes. In [81], the transmission of linear chirps (duration $= 5\ \mu$s, bandwidth $= 3$ MHz), instead of standard sinusoidal bursts, from a 256-element spiral probe yielded an SNR increase of 11.4 dB in 3-D Doppler applications. The efficacy of such a method can be appreciated by noting that the same SNR improvement could be obtained by quadruplicating the number of transmitting elements.

Similarly, advanced beamforming schemes developed to reduce imaging artifacts and improve the spatial resolution could be used to counteract the limited imaging contrast achievable by sparse arrays. In [107], for example, spatial coherence beamforming was exploited to achieve high-quality, HFR, volumetric contrast images, and increase the detectability of single microbubbles.

V. Conclusion

Most sparse array implementations have been obtained through a selection of elements out of a full gridded array. This means that in many cases the selected elements have positions associated with fabrication constraints, which may be different from the ideal ones. Although in principle, thanks to laser cutting, even the piezoelectric arrays could be arbitrarily positioned, in practice, for cost reasons, this possibility is currently restricted to arrays based on micromachined ultrasound transducers [140], [141], whose fabrication exploits integrated circuits technologies. Considering the increasing interest in sparse arrays, it is likely that micromachined transducers will become more and more important in this field.

In conclusion, sparse arrays are not expected to produce images with the same top quality as those produced by dense arrays having the same aperture and element size. However, they can be designed to produce images with good quality while avoiding the need for expensive ASICs or cumbersome cable connections to complex high channel count scanners [10], [13]. The highest expectations for sparse arrays are located at the convergence of three fields of research: 1) optimal layout definition; 2) improvement of individual element sensitivity; and 3) application-specific imaging technique. Sparse arrays will likely be increasingly used in association with open scanners for the experimental test and, when the SNR will be sufficiently improved, for the clinical application of novel 3-D imaging methods [80], [81]. In perspective, once their SNR be properly improved, they even represent a feasible option for the development of 3-D imaging and Doppler systems at a moderate cost and preclinical application of novel methods.

References

[1] A. Fenster, D. B. Downey, and H. N. Cardinal, "Three-dimensional ultrasound imaging," *Phys. Med. Biol.*, vol. 46, no. 5, pp. R67–R99, May 2001, doi: 10.1088/0031-9155/46/5/201.

[2] J. D. Larson, "2-D phased array ultrasound imaging system with distributed phasing," U.S. Patent 5 229 933 A, Jul. 20, 1993.

[3] B. Savord and R. Solomon, "Fully sampled matrix transducer for real time 3D ultrasonic imaging," in *Proc. IEEE Symp. Ultrason.*, vol. 1, Oct. 2003, pp. 945–953, doi: 10.1109/ULTSYM.2003.1293556.

[4] S. Blaak *et al.*, "Design of a micro-beamformer for a 2D piezoelectric ultrasound transducer," in *Proc. IEEE Int. Ultrason. Symp.*, Sep. 2009, pp. 1338–1341, doi: 10.1109/ULTSYM.2009.5441534.

[5] G. Matrone, A. S. Savoia, M. Terenzi, G. Caliano, F. Quaglia, and G. Magenes, "A volumetric CMUT-based ultrasound imaging system simulator with integrated reception and μ-beamforming electronics models," *IEEE Trans. Ultrason., Ferroelectr., Freq. Control*, vol. 61, no. 5, pp. 792–804, May 2014, doi: 10.1109/TUFFC.2014.2971.

[6] C. Chen *et al.*, "A front-end ASIC with receive sub-array beamforming integrated with a 32×32 PZT matrix transducer for 3-D transesophageal echocardiography," *IEEE J. Solid-State Circuits*, vol. 52, no. 4, pp. 994–1006, Apr. 2017, doi: 10.1109/JSSC.2016.2638433.

[7] J. Janjic *et al.*, "A 2-D ultrasound transducer with front-end ASIC and low cable count for 3-D forward-looking intravascular imaging: Performance and characterization," *IEEE Trans. Ultrason., Ferroelectr., Freq. Control*, vol. 65, no. 10, pp. 1832–1844, Oct. 2018, doi: 10.1109/TUFFC.2018.2859824.

[8] *xMATRIX Ultrasound Technology | Philips Ultrasound*. Philips. Accessed: May 27, 2-21. [Online]. Available: https://www.usa.philips.com/healthcare/resources/feature-detail/xmatrix

[9] *VividTM Ultra Edition Experience–Vivid E95*. Accessed: May 27, 2021. [Online]. Available: https://gevividultraedition.com/vivid-e95

[10] J. A. Jensen *et al.*, "SARUS: A synthetic aperture real-time ultrasound system," *IEEE Trans. Ultrason., Ferroelectr., Freq. Control*, vol. 60, no. 9, pp. 1838–1852, Sep. 2013, doi: 10.1109/TUFFC.2013.2770.

[11] E. Boni, A. C. H. Yu, S. Freear, J. A. Jensen, and P. Tortoli, "Ultrasound open platforms for next-generation imaging technique development," *IEEE Trans. Ultrason., Ferroelectr., Freq. Control*, vol. 65, no. 7, pp. 1078–1092, Jul. 2018, doi: 10.1109/TUFFC.2018.2844560.

[12] J. Provost, C. Papadacci, C. Demene, J.-L. Gennisson, M. Tanter, and M. Pernot, "3-D ultrafast Doppler imaging applied to the non-invasive mapping of blood vessels *in vivo*," *IEEE Trans. Ultrason., Ferroelectr., Freq. Control*, vol. 62, no. 8, pp. 1467–1472, Aug. 2015, doi: 10.1109/TUFFC.2015.007032.

[13] L. Petrusca *et al.*, "Fast volumetric ultrasound B-mode and Doppler imaging with a new high-channels density platform for advanced 4D cardiac imaging/therapy," *Appl. Sci.*, vol. 8, no. 2, p. 200, Feb. 2018, doi: 10.3390/app8020200.

[14] D. Mazierli, A. Ramalli, E. Boni, and F. Guidi, "Architecture for an ultrasound advanced open platform with an arbitrary number of independent channels," *IEEE Trans. Biomed. Circuits Syst.*, vol. 15, no. 3, pp. 486–496, Jun. 2021, doi: 10.1109/TBCAS.2021.3077664.

[15] C. Risser *et al.*, "Real-time volumetric ultrasound research platform with 1024 parallel transmit and receive channels," *Appl. Sci.*, vol. 11, no. 13, p. 5795, Jan. 2021, doi: 10.3390/app11135795.

[16] M. Pappalardo *et al.*, "Bidimensional ultrasonic array for volumetric imaging," U.S. Patent 2 008 083 876 A3, Sep. 25, 2008. Accessed: May 20, 2020. [Online]. Available: https://patents.google.com/patent/WO2008083876A3/it

[17] C. H. Seo and J. T. Yen, "A 256×256 2-D array transducer with row-column addressing for 3-D rectilinear imaging," *IEEE Trans. Ultrason., Ferroelectr., Freq. Control*, vol. 56, no. 4, pp. 837–847, Apr. 2009, doi: 10.1109/TUFFC.2009.1107.

[18] A. Sampaleanu, P. Zhang, A. Kshirsagar, W. Moussa, and R. J. Zemp, "Top-orthogonal-to-bottom-electrode (TOBE) CMUT arrays for 3-D ultrasound imaging," *IEEE Trans. Ultrason., Ferroelectr., Freq. Control*, vol. 61, no. 2, pp. 266–276, Feb. 2014, doi: 10.1109/TUFFC.2014.6722612.

[19] M. F. Rasmussen, T. L. Christiansen, E. V. Thomsen, and J. A. Jensen, "3-D imaging using row-column-addressed arrays with integrated apodization—Part i: Apodization design and line element beamforming," *IEEE Trans. Ultrason., Ferroelectr., Freq. Control*, vol. 62, no. 5, pp. 947–958, May 2015, doi: 10.1109/TUFFC.2014.006531.

[20] H. Bouzari *et al.*, "Curvilinear 3-D imaging using row-column-addressed 2-D arrays with a diverging lens: Feasibility study," *IEEE Trans. Ultrason., Ferroelectr., Freq. Control*, vol. 64, no. 6, pp. 978–988, Jun. 2017, doi: 10.1109/TUFFC.2017.2687521.

[21] D. King, R. Packard, and R. Thomas, "Unequally-spaced, broadband antenna arrays," *IRE Trans. Antennas Propag.*, vol. 8, no. 4, pp. 380–384, Jul. 1960, doi: 10.1109/TAP.1960.1144876.

[22] R. M. Leahy and B. D. Jeffs, "On the design of maximally sparse beamforming arrays," *IEEE Trans. Antennas Propag.*, vol. 39, no. 8, pp. 1178–1187, Aug. 1991, doi: 10.1109/8.97353.

[23] D. H. Turnbull and F. S. Foster, "Beam steering with pulsed two-dimensional transducer arrays," *IEEE Trans. Ultrason., Ferroelectr., Freq. Control*, vol. 38, no. 4, pp. 320–333, Jul. 1991, doi: 10.1109/58.84270.

[24] R. E. Davidsen, J. A. Jensen, and S. W. Smith, "Two-dimensional random arrays for real time volumetric imaging," *Ultrason. Imag.*, vol. 16, no. 3, pp. 143–163, Jul. 1994.

[25] S. W. Smith, R. E. Davidsen, C. D. Emery, R. L. Goldberg, and E. D. Light, "Update on 2-D array transducers for medical ultrasound," in *Proc. IEEE Ultrason. Symp. Int. Symp.*, vol. 2, Nov. 1995, pp. 1273–1278, doi: 10.1109/ULTSYM.1995.495789.

[26] J. L. Schwartz and B. D. Steinberg, "Ultrasparse, ultrawideband arrays," *IEEE Trans. Ultrason., Ferroelectr., Freq. Control*, vol. 45, no. 2, pp. 376–393, Mar. 1998, doi: 10.1109/58.660149.

[27] A. Austeng and S. Holm, "Sparse 2-D arrays for 3-D phased array imaging–design methods," *IEEE Trans. Ultrason., Ferroelectr., Freq. Control*, vol. 49, no. 8, pp. 1073–1086, Aug. 2002, doi: 10.1109/TUFFC.2002.1026019.

[28] P. K. Weber, R. M. Schmitt, B. D. Tylkowski, and J. Steck, "Optimization of random sparse 2-D transducer arrays for 3-D electronic beam steering and focusing," in *Proc. IEEE Ultrason. Symp. (ULTSYM)*, vol. 3, Oct./Nov. 1994, pp. 1503–1506, doi: 10.1109/ULTSYM.1994.401875.

[29] R. L. Haupt, "Thinned arrays using genetic algorithms," *IEEE Trans. Antennas Propag.*, vol. 42, no. 7, pp. 993–999, Jul. 1994, doi: 10.1109/8.299602.

[30] A. Austeng, S. Holm, P. K. Weber, N. Aakvaag, and K. Iranpour, "1D and 2D algorithmically optimized sparse arrays," in *Proc. IEEE Ultrason. Symp. Int. Symp.*, vol. 2, Oct. 1997, pp. 1683–1686, doi: 10.1109/ULTSYM.1997.663319.

[31] S. Holm and B. Elgetun, "Optimization of the beampattern of 2D sparse arrays by weighting," in *Proc. IEEE Ultrason. Symp. Int. Symp.*, vol. 2, Nov. 1995, pp. 1345–1348, doi: 10.1109/ULTSYM.1995.495805.

[32] V. Murino, A. Trucco, and C. S. Regazzoni, "Synthesis of unequally spaced arrays by simulated annealing," *IEEE Trans. Signal Process.*, vol. 44, no. 1, pp. 119–122, Jan. 1996, doi: 10.1109/78.482017.

[33] A. Trucco, "Thinning and weighting of large planar arrays by simulated annealing," *IEEE Trans. Ultrason., Ferroelectr., Freq. Control*, vol. 46, no. 2, pp. 347–355, Mar. 1999, doi: 10.1109/58.753023.

[34] S. Holm, A. Austeng, K. Iranpour, and J.-F. Hopperstad, "Sparse sampling in array processing," in *Nonuniform Sampling: Theory and Practice*, F. Marvasti, Ed. Boston, MA, USA: Springer, 2001, pp. 787–833, doi: 10.1007/978-1-4615-1229-5_19.

[35] J. W. Choe, O. Oralkan, and P. T. Khuri-Yakub, "Design optimization for a 2-D sparse transducer array for 3-D ultrasound imaging," in *Proc. IEEE Int. Ultrason. Symp.*, Oct. 2010, pp. 1928–1931, doi: 10.1109/ULTSYM.2010.5935854.

[36] P. Chen, B. Shen, L. Zhou, and Y. Chen, "Optimized simulated annealing algorithm for thinning and weighting large planar arrays," *J. Zhejiang Univ. Sci. C*, vol. 11, no. 4, pp. 261–269, 2010, doi: 10.1631/jzus.C0910037.

[37] C. Tekes, M. Karaman, and F. Degertekin, "Optimizing circular ring arrays for forward- looking IVUS imaging," *IEEE Trans. Ultrason., Ferroelectr., Freq. Control*, vol. 58, no. 12, pp. 2596–2607, Dec. 2011, doi: 10.1109/TUFFC.2011.2123.

[38] B. Diarra, M. Robini, P. Tortoli, C. Cachard, and H. Liebgott, "Design of optimal 2-D nongrid sparse arrays for medical ultrasound," *IEEE Trans. Biomed. Eng.*, vol. 60, no. 11, pp. 3093–3102, Nov. 2013, doi: 10.1109/TBME.2013.2267742.

[39] C. Sciallero and A. Trucco, "Design of a sparse planar array for optimized 3D medical ultrasound imaging," in *Proc. 23rd Eur. Signal Process. Conf. (EUSIPCO)*, Aug. 2015, pp. 1341–1345, doi: 10.1109/EUSIPCO.2015.7362602.

[40] C. Sciallero and A. Trucco, "Wideband 2-D sparse array optimization combined with multiline reception for real-time 3-D medical ultrasound," *Ultrasonics*, vol. 111, Mar. 2021, Art. no. 106318, doi: 10.1016/j.ultras.2020.106318.

[41] S. Kirkpatrick, C. D. Gelatt, and M. P. Vecchi, "Optimization by simulated annealing," *Science*, vol. 220, no. 4598, pp. 671–680, 1983, doi: 10.1126/science.220.4598.671.

[42] S. W. Smith, H. G. Pavy, and O. T. von Ramm, "High-speed ultrasound volumetric imaging system. I. Transducer design and beam steering," *IEEE Trans. Ultrason., Ferroelectr., Freq. Control*, vol. 38, no. 2, pp. 100–108, Mar. 1991, doi: 10.1109/58.68466.

[43] G. R. Lookwood and F. S. Foster, "Optimizing sparse two-dimensional transducer arrays using an effective aperture approach," in *Proc. IEEE Ultrason. Symp. (ULTSYM)*, vol. 3, Oct./Nov. 1994, pp. 1497–1501, doi: 10.1109/ULTSYM.1994.401874.

[44] G. R. Lookwood and F. S. Foster, "Optimizing the radiation pattern of sparse periodic two-dimensional arrays," *IEEE Trans. Ultrason., Ferroelectr., Freq. Control*, vol. 43, no. 1, pp. 15–19, Jan. 1996, doi: 10.1109/58.484458.

[45] S. I. Nikolov and J. A. Jensen, "Application of different spatial sampling patterns for sparse array transducer design," *Ultrasonics*, vol. 37, no. 10, pp. 667–671, Jul. 2000, doi: 10.1016/S0041-624X(00)00013-5.

[46] T. S. Sumanaweera, J. Schwartz, and D. Napolitano, "A spiral 2D phased array for 3D imaging," in *Proc. IEEE Ultrason. Symp. Int. Symp.*, vol. 2, Oct. 1999, pp. 1271–1274, doi: 10.1109/ULTSYM.1999.849228.

[47] O. Martínez-Graullera, C. J. Martín, G. Godoy, and L. G. Ullate, "2D array design based on Fermat spiral for ultrasound imaging," *Ultrasonics*, vol. 50, no. 2, pp. 280–289, 2010, doi: 10.1016/j.ultras.2009.09.010.

[48] A. Ramalli, E. Boni, A. S. Savoia, and P. Tortoli, "Density-tapered spiral arrays for ultrasound 3-D imaging," *IEEE Trans. Ultrason., Ferroelectr., Freq. Control*, vol. 62, no. 8, pp. 1580–1588, Aug. 2015, doi: 10.1109/TUFFC.2015.007035.

[49] H. Yoon and T.-K. Song, "Sparse rectangular and spiral array designs for 3D medical ultrasound imaging," *Sensors*, vol. 20, no. 1, p. 173, Dec. 2019, doi: 10.3390/s20010173.

[50] C. Boni, M. Richard, and S. Barbarossa, "Optimal configuration and weighting of nonuniform arrays according to a maximum ISLR criterion," in *Proc. IEEE Int. Conf. Acoust., Speech Signal Process. (ICASSP)*, vol. 5, 1994, pp. V/157–V/160, doi: 10.1109/ICASSP.1994.389424.

[51] S. Holm, B. Elgetun, and G. Dahl, "Properties of the beampattern of weight- and layout-optimized sparse arrays," *IEEE Trans. Ultrason., Ferroelectr., Freq. Control*, vol. 44, no. 5, pp. 983–991, Sep. 1997, doi: 10.1109/58.655623.

[52] H. Zhang, B. Bai, J. Zheng, and Y. Zhou, "Optimal design of sparse array for ultrasonic total focusing method by binary particle swarm optimization," *IEEE Access*, vol. 8, pp. 111945–111953, 2020, doi: 10.1109/ACCESS.2020.3001947.

[53] B. D. Steinberg, *Principles of Aperture and Array System Design: Including Random and Adaptive Arrays*. New York, NY, USA: Wiley, 1976.

[54] M. Pappalardo, G. Caliano, A. S. Savoia, and A. Caronti, "Micromachined ultrasonic transducers," in *Piezoelectric and Acoustic Materials for Transducer Applications*, A. Safari E. K. Akdoğan, Eds. Boston, MA, USA: Springer, 2008, pp. 453–478, doi: 10.1007/978-0-387-76540-2_22.

[55] J. W. Goodman, *Introduction to Fourier Optics*. New York, NY, USA: McGraw-Hill, 1968.

[56] T. L. Szabo, *Diagnostic Ultrasound Imaging: Inside Out*, 1st ed. New York, NY, USA: Academic, 2004.

[57] R. Cohen and Y. C. Eldar, "Sparse array design via fractal geometries," *IEEE Trans. Signal Process.*, vol. 68, pp. 4797–4812, 2020, doi: 10.1109/TSP.2020.3016772.

[58] Ó. Martínez-Graullera, J. C. E. de Souza, M. Parrilla Romero, and R. T. Higuti, "Design of 2D planar sparse binned arrays based on the coarray analysis," *Sensors*, vol. 21, no. 23, p. 8018, Nov. 2021, doi: 10.3390/s21238018.

[59] J. A. Jensen, "Simulation of advanced ultrasound systems using field II," in *Proc. 2nd IEEE Int. Symp. Biomed. Imag., Nano Macro*, vol. 1, Apr. 2004, pp. 636–639, doi: 10.1109/ISBI.2004.1398618.

[60] B. E. Treeby and B. T. Cox, "K-wave: MATLAB toolbox for the simulation and reconstruction of photoacoustic wave fields," *J. Biomed. Opt.*, vol. 15, no. 2, Mar. 2010, Art. no. 021314, doi: 10.1117/1.3360308.

[61] D. Chen and R. J. McGough, "A 2D fast near-field method for calculating near-field pressures generated by apodized rectangular pistons," *J. Acoust. Soc. Amer.*, vol. 124, no. 3, pp. 1526–1537, Sep. 2008, doi: 10.1121/1.2950081.

[62] M. Karaman, I. O. Wygant, Ö. Oralkan, and B. T. Khuri-Yakub, "Minimally redundant 2-D array designs for 3-D medical ultrasound imaging," *IEEE Trans. Med. Imag.*, vol. 28, no. 7, pp. 1051–1061, Jul. 2009, doi: 10.1109/TMI.2008.2010936.

[63] E. Roux, A. Ramalli, H. Liebgott, C. Cachard, M. C. Robini, and P. Tortoli, "Wideband 2-D array design optimization with fabrication constraints for 3-D U.S. imaging," *IEEE Trans. Ultrason., Ferroelectr., Freq. Control*, vol. 64, no. 1, pp. 108–125, Jan. 2017, doi: 10.1109/TUFFC.2016.2614776.

[64] E. Roux, A. Ramalli, P. Tortoli, C. Cachard, M. Robini, and H. Liebgott, "2-D ultrasound sparse arrays multidepth radiation optimization using simulated annealing and spiral-array inspired energy functions," *IEEE Trans. Ultrason., Ferroelectr., Freq. Control*, vol. 63, no. 12, pp. 2138–2149, Dec. 2016, doi: 10.1109/TUFFC.2016.2602242.

[65] B. Diarra *et al.*, "Feasibility of genetic algorithms in 2D ultrasound array optimization," in *Proc. IEEE Int. Ultrason. Symp. (IUS)*, Oct. 2018, pp. 1–9, doi: 10.1109/ULTSYM.2018.8579952.

[66] P. J. M. van Laarhoven and E. H. L. Aarts, "Simulated annealing," in *Simulated Annealing: Theory and Applications*, P. J. M. van Laarhoven E. H. L. Aarts, Eds. Dordrecht, The Netherlands: Springer, 1987, pp. 7–15, doi: 10.1007/978-94-015-7744-1_2.

[67] M. C. Robini, "Theoretically grounded acceleration techniques for simulated annealing," in *Handbook Optimization: From Classical to Modern Approach*, I. Zelinka, V. Snášel, A. Abraham, Eds. Berlin, Germany: Springer, 2013, pp. 311–335, doi: 10.1007/978-3-642-30504-7_13.

[68] Q. Zhang *et al.*, "Multiple focus patterns of sparse random array using particles swarm optimization for ultrasound surgery," *IEEE Trans. Ultrason., Ferroelectr., Freq. Control*, vol. 69, no. 2, pp. 565–579, Feb. 2022, doi: 10.1109/TUFFC.2021.3127222.

[69] J. Kennedy and R. Eberhart, "Particle swarm optimization," in *Proc. Int. Conf. Neural Netw. (ICNN)*, vol. 4, Dec. 1995, pp. 1942–1948, doi: 10.1109/ICNN.1995.488968.

[70] S. S. Brunke and G. R. Lockwood, "Broad-bandwidth radiation patterns of sparse two-dimensional Vernier arrays," *IEEE Trans. Ultrason., Ferroelectr., Freq. Control*, vol. 44, no. 5, pp. 1101–1109, Sep. 1997, doi: 10.1109/58.655635.

[71] J. T. Yen, J. P. Steinberg, and S. W. Smith, "Sparse 2-D array design for real time rectilinear volumetric imaging," *IEEE Trans. Ultrason., Ferroelectr., Freq. Control*, vol. 47, no. 1, pp. 93–110, Jan. 2000, doi: 10.1109/58.818752.

[72] W. J. Hendricks, "The totally random versus the bin approach for random arrays," *IEEE Trans. Antennas Propag.*, vol. 39, no. 12, pp. 1757–1762, Dec. 1991, doi: 10.1109/8.121597.

[73] M. C. Vigano, G. Toso, G. Caille, C. Mangenot, and I. E. Lager, "Spatial density tapered sunflower antenna array," in *Proc. 3rd Eur. Conf. Antennas Propag. (EUCAP)*, Mar. 2009, pp. 778–782.

[74] M. C. Viganó, G. Toso, G. Caille, C. Mangenot, and I. E. Lager, "Sunflower array antenna with adjustable density taper," *Int. J. Antennas Propag.*, vol. 2009, Apr. 2009, Art. no. 624035, doi: 10.1155/2009/624035.

[75] S. Nooijens, A. Ramalli, M. Ingram, M. Fournelle, A. Bertrand, and J. D'hooge, "Design of a sparse ellipsoidal array for volumetric ultrasound imaging of the prostate," in *Proc. IEEE Int. Ultrason. Symp. (IUS)*, Sep. 2020, pp. 1–3, doi: 10.1109/IUS46767.2020.9251385.

[76] E. D. Light, R. E. Davidsen, J. O. Fiering, T. A. Hruschka, and S. W. Smith, "Progress in two-dimensional arrays for real-time volumetric imaging," *Ultrason. Imag.*, vol. 20, no. 1, pp. 1–15, Jan. 1998, doi: 10.1177/016173469802000101.

[77] A. Austeng and S. Holm, "Sparse 2-D arrays for 3-D phased array imaging-experimental validation," *IEEE Trans. Ultrason., Ferroelectr., Freq. Control*, vol. 49, no. 8, pp. 1087–1093, Aug. 2002, doi: 10.1109/TUFFC.2002.1026020.

[78] M. F. Rasmussen and J. A. Jensen, "3-D ultrasound imaging performance of a row-column addressed 2-D array transducer: A measurement study," in *Proc. IEEE Int. Ultrason. Symp. (IUS)*, Jul. 2013, pp. 1460–1463, doi: 10.1109/ULTSYM.2013.0370.

[79] S. Harput *et al.*, "3-D super-resolution ultrasound imaging with a 2-D sparse array," *IEEE Trans. Ultrason., Ferroelectr., Freq. Control*, vol. 67, no. 2, pp. 269–277, Feb. 2020, doi: 10.1109/TUFFC.2019.2943646.

[80] A. Ramalli *et al.*, "High-frame-rate tri-plane echocardiography with spiral arrays: From simulation to real-time implementation," *IEEE Trans. Ultrason., Ferroelectr., Freq. Control*, vol. 67, no. 1, pp. 57–69, Jan. 2020, doi: 10.1109/TUFFC.2019.2940289.

[81] A. Ramalli *et al.*, "Real-time 3-D spectral Doppler analysis with a sparse spiral array," *IEEE Trans. Ultrason., Ferroelectr., Freq. Control*, vol. 68, no. 5, pp. 1742–1751, May 2021, doi: 10.1109/TUFFC.2021.3051628.

[82] E. Roux, F. Varray, L. Petrusca, C. Cachard, P. Tortoli, and H. Liebgott, "Experimental 3-D ultrasound imaging with 2-D sparse arrays using focused and diverging waves," *Sci. Rep.*, vol. 8, no. 1, p. 9108, 2018, doi: 10.1038/s41598-018-27490-2.

[83] E. Boni, A. Ramalli, V. Daeichin, N. de Jong, H. J. Vos, and P. Tortoli, "Prototype 3D real-time imaging system based on a sparse PZT spiral array," in *Proc. IEEE Int. Ultrason. Symp. (IUS)*, Oct. 2018, pp. 1–4, doi: 10.1109/ULTSYM.2018.8580133.

[84] H. J. Vos *et al.*, "Sparse volumetric PZT array with density tapering," in *Proc. IEEE Int. Ultrason. Symp. (IUS)*, Oct. 2018, pp. 1–4, doi: 10.1109/ULTSYM.2018.8580197.

[85] E. Boni, F. Fool, M. D. Verweij, H. J. Vos, and P. Tortoli, "On the efficacy of in-probe pre-amplifiers for piezoelectric 2D arrays," in *Proc. IEEE Int. Ultrason. Symp. (IUS)*, Sep. 2020, pp. 1–4, doi: 10.1109/IUS46767.2020.9251800.

[86] X. Li, A. Gachagan, and P. Murray, "Design of 2D sparse array transducers for anomaly detection in medical phantoms," *Sensors*, vol. 20, no. 18, p. 5370, Jan. 2020, doi: 10.3390/s20185370.

[87] W. Y. Choi, Y. S. Kwak, and K. K. Park, "3-D synthetic imaging using 128-channel 2-D sparse CMUT array," in *Proc. IEEE Int. Ultrason. Symp. (IUS)*, Sep. 2017, pp. 1–4, doi: 10.1109/ULTSYM.2017.8091927.

[88] K. K. Park, H. Lee, M. Kupnik, and B. T. Khuri-Yakub, "Fabrication of capacitive micromachined ultrasonic transducers via local oxidation and direct wafer bonding," *J. Microelectromech. Syst.*, vol. 20, no. 1, pp. 95–103, Feb. 2011, doi: 10.1109/JMEMS.2010.2093567.

[89] A. Stuart Savoia *et al.*, "A 256-element spiral CMUT array with integrated analog front end and transmit beamforming circuits," in *Proc. IEEE Int. Ultrason. Symp. (IUS)*, Oct. 2018, pp. 206–212, doi: 10.1109/ULTSYM.2018.8579867.

[90] A. S. Savoia, G. Caliano, and M. Pappalardo, "A CMUT probe for medical ultrasonography: From microfabrication to system integration," *IEEE Trans. Ultrason., Ferroelectr., Freq. Control*, vol. 59, no. 6, pp. 1127–1138, Jun. 2012, doi: 10.1109/TUFFC.2012.2303.

[91] A. S. Savoia *et al.*, "A 3D packaging technology for acoustically optimized integration of 2D CMUT arrays and front end circuits," in *Proc. IEEE Int. Ultrason. Symp. (IUS)*, Sep. 2017, pp. 1–4, doi: 10.1109/ULTSYM.2017.8092991.

[92] C. Tekes *et al.*, "Experimental study of dual-ring CMUT array optimization for forward-looking IVUS," in *Proc. IEEE Int. Ultrason. Symp.*, Oct. 2011, pp. 1127–1130, doi: 10.1109/ULTSYM.2011.0277.

[93] Y. Wang, D. N. Stephens, and M. O'Donnell, "Optimizing the beam pattern of a forward-viewing ring-annular ultrasound array for intravascular imaging," *IEEE Trans. Ultrason., Ferroelectr., Freq. Control*, vol. 49, no. 12, pp. 1652–1664, Dec. 2002, doi: 10.1109/TUFFC.2002.1159845.

[94] D. T. Yeh, O. Oralkan, I. O. Wygant, M. O'Donnell, and B. T. Khuri-Yakub, "3-D ultrasound imaging using a forward-looking CMUT ring array for intravascular/intracardiac applications," *IEEE Trans. Ultrason., Ferroelectr., Freq. Control*, vol. 53, no. 6, pp. 1202–1211, Jun. 2006, doi: 10.1109/TUFFC.2006.1642519.

[95] E. Boni *et al.*, "Architecture of an ultrasound system for continuous real-time high frame rate imaging," *IEEE Trans. Ultrason., Ferroelectr., Freq. Control*, vol. 64, no. 9, pp. 1276–1284, Sep. 2017, doi: 10.1109/TUFFC.2017.2727980.

[96] B. Heyde *et al.*, "Regional cardiac motion and strain estimation in three-dimensional echocardiography: A validation study in thick-walled univentricular phantoms," *IEEE Trans. Ultrason., Ferroelectr., Freq. Control*, vol. 59, no. 4, pp. 668–682, Apr. 2012, doi: 10.1109/TUFFC.2012.2245.

[97] P. Mattesini, A. Ramalli, L. Petrusca, O. Basset, H. Liebgott, and P. Tortoli, "Spectral Doppler measurements with 2-D sparse arrays," *IEEE Trans. Ultrason., Ferroelectr., Freq. Control*, vol. 67, no. 2, pp. 278–285, Feb. 2020, doi: 10.1109/TUFFC.2019.2944090.

[98] S. Rossi, A. Ramalli, F. Fool, and P. Tortoli, "High-frame-rate 3-D vector flow imaging in the frequency domain," *Appl. Sci.*, vol. 10, no. 15, p. 5365, Aug. 2020, doi: 10.3390/app10155365.

[99] S. W. Smith, K. Chu, S. F. Idriss, N. M. Ivancevich, E. D. Light, and P. D. Wolf, "Feasibility study: Real-time 3-D ultrasound imaging of the brain," *Ultrasound Med. Biol.*, vol. 30, no. 10, pp. 1365–1371, Oct. 2004, doi: 10.1016/j.ultrasmedbio.2004.08.012.

[100] N. M. Ivancevich, G. F. Pinton, H. A. Nicoletto, E. Bennett, D. T. Laskowitz, and S. W. Smith, "Real-time 3-D contrast-enhanced transcranial ultrasound and aberration correction," *Ultrasound Med. Biol.*, vol. 34, no. 9, pp. 1387–1395, Sep. 2008, doi: 10.1016/j.ultrasmedbio.2008.01.015.

[101] S. W. Smith *et al.*, "The ultrasound brain helmet: Feasibility study of multiple simultaneous 3D scans of cerebral vasculature," *Ultrasound iMed. Biol.*, vol. 35, no. 2, pp. 329–338, Feb. 2009, doi: 10.1016/j.ultrasmedbio.2008.08.016.

[102] B. D. Lindsey, E. D. Light, H. A. Nicoletto, E. R. Bennett, D. T. Laskowitz, and S. W. Smith, "The ultrasound brain helmet: New transducers and volume registration for *in vivo* simultaneous multi-transducer 3-D transcranial imaging," *IEEE Trans. Ultrason., Ferroelectr., Freq. Control*, vol. 58, no. 6, pp. 1189–1202, Jun. 2011, doi: 10.1109/TUFFC.2011.1929.

[103] M. A. O'Reilly and K. Hynynen, "A super-resolution ultrasound method for brain vascular mapping," *Med. Phys.*, vol. 40, no. 11, p. 110701, Nov. 2013, doi: 10.1118/1.4823762.

[104] J. Song and K. Hynynen, "Feasibility of using lateral mode coupling method for a large scale ultrasound phased array for noninvasive transcranial therapy," *IEEE Trans. Biomed. Eng.*, vol. 57, no. 1, pp. 124–133, Jan. 2010, doi: 10.1109/TBME.2009.2028739.

[105] A. Stanziola, C. H. Leow, E. Bazigou, P. D. Weinberg, and M.-X. Tang, "ASAP: Super-contrast vasculature imaging using coherence analysis and high frame-rate contrast enhanced ultrasound," *IEEE Trans. Med. Imag.*, vol. 37, no. 8, pp. 1847–1856, Aug. 2018, doi: 10.1109/TMI.2018.2798158.

[106] S. Harput *et al.*, "Quantitative microvessel analysis with 3-D super-resolution ultrasound and velocity mapping," in *Proc. IEEE Int. Ultrason. Symp. (IUS)*, Sep. 2020, pp. 1–4, doi: 10.1109/IUS46767.2020.9251336.

[107] L. Wei *et al.*, "High frame rate volumetric imaging of microbubbles using a sparse array and spatial coherence beamforming," *IEEE Trans. Ultrason., Ferroelectr., Freq. Control*, vol. 68, no. 10, pp. 3069–3081, Oct. 2021, doi: 10.1109/TUFFC.2021.3086597.

[108] M. Xu and L. V. Wang, "Photoacoustic imaging in biomedicine," *Rev. Sci. Instrum.*, vol. 77, no. 4, Sep. 2006, Art. no. 041101, doi: 10.1063/1.2195024.

[109] P. Beard, "Biomedical photoacoustic imaging," *Interface Focus*, vol. 1, no. 4, pp. 602–631, Aug. 2011, doi: 10.1098/rsfs.2011.0028.

[110] P. Ephrat, L. Keenliside, A. Seabrook, F. S. Prato, and J. J. Carson, "Three-dimensional photoacoustic imaging by sparse-array detection and iterative image reconstruction," *J. Biomed. Opt.*, vol. 13, no. 5, p. 054052, 2008, doi: 10.1117/1.2992131.

[111] G. Paltauf, J. A. Viator, S. A. Prahl, and S. L. Jacques, "Iterative reconstruction algorithm for optoacoustic imaging," *J. Acoust. Soc. Amer.*, vol. 112, no. 4, pp. 1536–1544, 2002, doi: 10.1121/1.1501898.

[112] H. Liebgott, A. Basarab, D. Kouame, O. Bernard, and D. Friboulet, "Compressive sensing in medical ultrasound," in *Proc. IEEE Int. Ultrason. Symp.*, Oct. 2012, pp. 1–6, doi: 10.1109/ULTSYM.2012.0486.

[113] M. Roumeliotis *et al.*, "Analysis of a photoacoustic imaging system by the crosstalk matrix and singular value decomposition," *Opt. Exp.*, vol. 18, no. 11, pp. 11406–11417, May 2010.

[114] M. B. Roumeliotis, R. Z. Stodilka, A. Mark Anastasio, E. Ng, and J. J. L. Carson, "Singular value decomposition analysis of a photoacoustic imaging system and 3D imaging at 0.7 FPS," *Opt. Exp.*, vol. 19, no. 14, pp. 13405–13417, Jun. 2011, doi: 10.1364/OE.19.013405.

[115] M. B. Roumeliotis, I. Kosik, and J. J. L. Carson, "3D photoacoustic imaging using a staring-sparse array with 60 transducers," *Proc. SPIE*, vol. 8223, Feb. 2012, Art. no. 82233F, doi: 10.1117/12.908841.

[116] M. Zafar, K. Kratkiewicz, R. Manwar, and M. Avanaki, "Development of low-cost fast photoacoustic computed tomography: System characterization and phantom study," *Appl. Sci.*, vol. 9, no. 3, p. 374, Jan. 2019, doi: 10.3390/app9030374.

[117] K. Kratkiewicz *et al.*, "Development of a stationary 3D photoacoustic imaging system using sparse single-element transducers: Phantom study," *Appl. Sci.*, vol. 9, no. 21, p. 4505, Oct. 2019, doi: 10.3390/app9214505.

[118] M. A. Kalkhoran and D. Vray, "Sparse sampling and reconstruction for an optoacoustic ultrasound volumetric hand-held probe," *Biomed. Opt. Exp.*, vol. 10, no. 4, pp. 1545–1556, Apr. 2019, doi: 10.1364/BOE.10.001545.

[119] M. A. Kalkhoran, F. Varray, A. S. Savoia, and D. Vray, "Sparse hand-held probe for optoacoustic ultrasound volumetric imaging: An experimental proof-of-concept study," *Opt. Lett.*, vol. 45, no. 4, pp. 885–888, Feb. 2020, doi: 10.1364/OL.384002.

[120] W. L. Nyborg, "Biological effects of ultrasound: Development of safety guidelines. Part II: General review," *Ultrasound Med. Biol.*, vol. 27, no. 3, pp. 301–333, Mar. 2001, doi: 10.1016/S0301-5629(00)00333-1.

[121] E. S. Ebbini and C. A. Cain, "Experimental evaluation of a prototype cylindrical section ultrasound hyperthermia phased-array applicator," *IEEE Trans. Ultrason., Ferroelectr., Freq. Control*, vol. 38, no. 5, pp. 510–520, Sep. 1991, doi: 10.1109/58.84298.

[122] S. A. Goss, L. A. Frizzell, J. T. Kouzmanoff, J. M. Barich, and J. M. Yang, "Sparse random ultrasound phased array for focal surgery," *IEEE Trans. Ultrason., Ferroelectr., Freq. Control*, vol. 43, no. 6, pp. 1111–1121, Nov. 1996, doi: 10.1109/58.542054.

[123] L. R. Gavrilov, J. W. Hand, and I. G. Yushina, "Two-dimensional phased arrays for application in surgery: Scanning by several focuses," *Acoust. Phys.*, vol. 46, no. 5, pp. 551–558, Sep. 2000, doi: 10.1134/1.1310379.

[124] M. Pernot, J.-F. Aubry, M. Tanter, J.-L. Thomas, and M. Fink, "High power transcranial beam steering for ultrasonic brain therapy," *Phys. Med. Biol.*, vol. 48, no. 16, pp. 2577–2589, 2003, doi: 10.1088/0031-9155/48/16/301.

[125] N. Ellens, A. Pulkkinen, J. Song, and K. Hynynen, "The utility of sparse 2D fully electronically steerable focused ultrasound phased arrays for thermal surgery: A simulation study," *Phys. Med. Biol.*, vol. 56, no. 15, pp. 4913–4932, Aug. 2011, doi: 10.1088/0031-9155/56/15/017.

[126] L. Deng, M. A. O'Reilly, R. M. Jones, R. An, and K. Hynynen, "A multi-frequency sparse hemispherical ultrasound phased array for microbubble-mediated transcranial therapy and simultaneous cavitation mapping," *Phys. Med. Biol.*, vol. 61, no. 24, pp. 8476–8501, Nov. 2016, doi: 10.1088/0031-9155/61/24/8476.

[127] C. Crake, S. T. Brinker, C. M. Coviello, M. S. Livingstone, and N. J. McDannold, "A dual-mode hemispherical sparse array for 3d passive acoustic mapping and skull localization within a clinical MRI guided focused ultrasound device," *Phys. Med. Biol.*, vol. 63, no. 6, 2018, Art. no. 065008, doi: 10.1088/1361-6560/aab0aa.

[128] P. Ramaekers, M. de Greef, R. Berriet, C. T. W. Moonen, and M. Ries, "Evaluation of a novel therapeutic focused ultrasound transducer based on Fermat's spiral," *Phys. Med. Biol.*, vol. 62, no. 12, pp. 5021–5045, 2017, doi: 10.1088/1361-6560/aa716c.

[129] P. B. Rosnitskiy, B. A. Vysokanov, L. R. Gavrilov, O. A. Sapozhnikov, and V. A. Khokhlova, "Method for designing multielement fully populated random phased arrays for ultrasound surgery applications," *IEEE Trans. Ultrason., Ferroelectr., Freq. Control*, vol. 65, no. 4, pp. 630–637, Apr. 2018, doi: 10.1109/TUFFC.2018.2800160.

[130] H. Bouzari, M. Engholm, S. I. Nikolov, M. B. Stuart, E. V. Thomsen, and J. A. Jensen, "Imaging performance for two row–column arrays," *IEEE Trans. Ultrason., Ferroelectr., Freq. Control*, vol. 66, no. 7, pp. 1209–1221, Jul. 2019, doi: 10.1109/TUFFC.2019.2914348.

[131] J. Hansen-Shearer, M. Lerendegui, M. Toulemonde, and M.-X. Tang, "Ultrafast 3-D ultrasound imaging using row–column array specific frame-multiply-and-sum beamforming," *IEEE Trans. Ultrason., Ferroelectr., Freq. Control*, vol. 69, no. 2, pp. 480–488, Feb. 2022, doi: 10.1109/TUFFC.2021.3122094.

[132] C. E. M. Demore, A. W. Joyce, K. Wall, and G. R. Lockwood, "Real-time volume imaging using a crossed electrode array," *IEEE Trans. Ultrason., Ferroelectr., Freq. Control*, vol. 56, no. 6, pp. 1252–1261, Jun. 2009, doi: 10.1109/TUFFC.2009.1167.

[133] M. Engholm, A. S. Havreland, E. V. Thomsen, C. Beers, B. G. Tomov, and J. A. Jensen, "A row-column-addressed 2D probe with an integrated compound diverging lens," in *Proc. IEEE Int. Ultrason. Symp. (IUS)*, Oct. 2018, pp. 1–4, doi: 10.1109/ULTSYM.2018.8579955.

[134] B. Diarra, M. Robini, H. Liebgott, C. Cachard, and P. Tortoli, "Variable-size elements in 2D sparse arrays for 3D medical ultrasound," in *Proc. IEEE Int. Ultrason. Symp. (IUS)*, Jul. 2013, pp. 508–511, doi: 10.1109/ULTSYM.2013.0132.

[135] C. D. Emery and S. W. Smith, "Improved signal-to-noise ratio in hybrid 2-D arrays: Experimental confirmation," *Ultrason. Imag.*, vol. 19, no. 2, pp. 93–111, Apr. 1997, doi: 10.1177/016173469701900201.

[136] T. Misaridis and J. A. Jensen, "Use of modulated excitation signals in medical ultrasound. Part I: Basic concepts and expected benefits," *IEEE Trans. Ultrason., Ferroelectr., Freq. Control*, vol. 52, no. 2, pp. 177–191, Feb. 2005, doi: 10.1109/TUFFC.2005.1406545.

[137] R. Y. Chiao and X. Hao, "Coded excitation for diagnostic ultrasound: A system developer's perspective," *IEEE Trans. Ultrason., Ferroelectr., Freq. Control*, vol. 52, no. 2, pp. 160–170, Feb. 2005, doi: 10.1109/TUFFC.2005.1406543.

[138] C. Yoon, W. Lee, J. H. Chang, T.-K. Song, and Y. Yoo, "An efficient pulse compression method of chirp-coded excitation in medical ultrasound imaging," *IEEE Trans. Ultrason., Ferroelectr., Freq. Control*, vol. 60, no. 10, pp. 2225–2229, Oct. 2013, doi: 10.1109/TUFFC.2013.2815.

[139] A. Ramalli, F. Guidi, E. Boni, and P. Tortoli, "A real-time chirp-coded imaging system with tissue attenuation compensation," *Ultrasonics*, vol. 60, pp. 65–75, Jul. 2015, doi: 10.1016/j.ultras.2015.02.013.

[140] P. Muralt *et al.*, "Piezoelectric micromachined ultrasonic transducers based on PZT thin films," *IEEE Trans. Ultrason., Ferroelectr., Freq. Control*, vol. 52, no. 12, pp. 2276–2288, Dec. 2005, doi: 10.1109/TUFFC.2005.1563270.

[141] D. E. Dausch, J. B. Castellucci, D. R. Chou, and O. T. von Ramm, "5I-4 piezoelectric micromachined ultrasound transducer (pMUT) arrays for 3D imaging probes," in *Proc. IEEE Ultrason. Symp.*, Oct. 2006, pp. 934–937, doi: 10.1109/ULTSYM.2006.248.

Alessandro Ramalli (Senior Member, IEEE) was born in Prato, Italy, in 1983. He received the master's degree in electronics engineering from the University of Florence, Florence, Italy, in 2008, and the joint Ph.D. degree in electronics system engineering and in automation, systems and images from the University of Florence and the University of Lyon, Lyon, France, in 2012.

From 2012 to 2017, he was involved in the development of the imaging section of a programmable open ultrasound system by the University of Florence. From 2017 to 2019, he worked as a Postdoctoral Researcher with the Laboratory of Cardiovascular Imaging and Dynamics, KU Leuven, Leuven, Belgium, granted by the European Commission through a "Marie Skłodowska-Curie Individual Fellowships." Here, he developed high frame rate imaging techniques for echocardiography. From 2020 to 2022, he worked as a Research Fellow at the University of Florence, where he is currently an Assistant Professor. His research interests include medical imaging, echocardiography, beamforming methods, ultrasound simulation, arrays, and systems design.

Enrico Boni (Member, IEEE) was born in Florence, Italy, in 1977. He received the master's degree in electronic engineering and the Ph.D. degree in electronic system engineering from the University of Florence, Florence, Italy, in 2001 and 2005, respectively.

Since December 2021, he has been an Associate Professor in electronics at the Department of Information Engineering, University of Florence. His research interests include analog and digital systems design, digital signal processing algorithms, digital control systems, Doppler ultrasound signal processing, microemboli detection and classification, ultrasound research platforms, and ultrasound frontend electronics design.

Emmanuel Roux received the joint Ph.D. degree in acoustics and information engineering from the University of Lyon, Lyon, France, and the University of Florence, Florence, Italy, in 2016.

He has been an Associate Professor at the Université Lyon 1, Lyon, and the CREATIS Laboratory, Lyon, since 2019. His current research concerns (deep) machine learning for medical imaging, with particular interests on 3-D ultrasound imaging (2-D transducer optimization and beamforming techniques), volumetric medical image segmentation (e.g., CT lungs or MRI lesion quantification), weakly-supervised anomaly detection (e.g., transcranial Doppler emboli classification), and interactive learning (model interpretability and interactive annotations).

Hervé Liebgott was a Full Professor at the University of Lyon, Lyon, France, in 2016. He has been the Leader of the Ultrasound Group at the CREATIS Laboratory, Lyon, since 2017. His research interest includes image and signal processing applied to medical ultrasound imaging. He is particularly interested in image formation techniques and motion estimation.

Dr. Liebgott became an elected member of the IEEE International Ultrasonics Symposium Technical Committee in 2014. He is currently the Group 1 Medical Ultrasonics TPC Co-Chair. From 2014 to 2016, he has served as an elected Associate Member for the IEEE Bio Imaging and Signal Processing (BISP) Technical Committee. He has served as an Associate Editor for the IEEE TRANSACTIONS ON ULTRASONICS, FERROELECTRICS, AND FREQUENCY CONTROL from 2015 to 2022.

Piero Tortoli (Fellow, IEEE) received the Laurea degree in electronics engineering from the University of Florence, Florence, Italy, in 1978.

Since then, he has been on the faculty of the Information Engineering Department, University of Florence, where he is currently a Full Professor of electronics and was elected member of the Academic Senate. He is leading the Microelectronics Systems Design Laboratory, Florence. His research interests include the development of open ultrasound research systems and novel imaging/Doppler methods. On these topics, he has authored more than 300 articles.

Prof. Tortoli is a fellow of AIMBE, "*Docteur Honoris causa*" of the University Claude Bernard Lyon 1, and an Honorary Member of the Polish Academy of Sciences. He has served on the IEEE International Ultrasonics Symposium Technical Program Committee since 1999. He chaired the 22nd International Symposium on Acoustical Imaging in 1995 and the 12th New England Doppler Conference in 2003, established the Artimino Conference on Medical Ultrasound Technology in 2011 and organized it again in 2017. He was an Associate Editor from 2013 to 2022 and a Guest Editor for three special issues of the IEEE TRANSACTIONS ON ULTRASONICS, FERROELECTRICS, AND FREQUENCY CONTROL in 2006, 2016, and 2018.